Spring 2016

Spatiotemporal Slip Rate Variations Along Surprise Valley Fault in Relation to Pleistocene Pluvial Lakes

Brian N. Marion
Central Washington University, marionb@cwu.edu

SPATIOTEMPORAL SLIP RATE VARIATIONS ALONG SURPRISE VALLEY FAULT IN RELATION TO PLEISTOCENE PLUVIAL LAKES

A Thesis

Presented to

The Graduate Faculty

Central Washington University

In Partial Fulfillment

of the Requirements for the Degree

Master of Science

Geological Sciences

---

by

Brian Nicholas Marion

May 2016

CENTRAL WASHINGTON UNIVERSITY

Graduate Studies

We hereby approve the thesis of

Brian Nicholas Marion

Candidate for the degree of Master of Science

APPROVED FOR THE GRADUATE FACULTY

_____ _____
Dr. Anne Egger, Committee Chair

_____ _____
Dr. Walter Szeliga

_____ _____
Dr. Lisa Ely

_____ _____
Dean of Graduate Studies

ABSTRACT

SPATIOTEMPORAL SLIP RATE VARIATIONS ALONG SURPRISE VALLEY FAULT IN RELATION TO PLEISTOCENE PLUVIAL LAKES

by

Brian Nicholas Marion

May 2016

Using mapped paleoshoreline features with high-resolution topographic data and obtained radiocarbon dates on paleoshoreline tufas, I documented precise fault offsets of dated features over the last 25 ka along the Surprise Valley Fault (SVF). Fault offset measured in three lake sections within Surprise Valley ranged from 3.6 m in the southern section to 14.4 m in the central section. The offset paleoshorelines are dated to the late Pleistocene (<22 ka) and were formed during the latest impoundment of pluvial Lake Surprise since the last glacial maximum. Slip rates vary along strike, assuming a fault dip of 68° with 0.25 ± 0.02 mm/yr in the northern section, 1.07 ± 0.10 mm/yr in the central section, and 0.36 ± 0.04 mm/yr in the southern lake section. Potential field modeling of profiles drawn through detailed, gridded gravity and magnetic data, suggest that the surficial scarps continue at depth, where they may accommodate greater offset. These results refine the time-averaged slip rate along the SVF and show variability spatially and temporally, allowing for correlations with changes in paleolake levels. This study suggest

complex relation between pluvial lakes and their proximal faults that show that the lake likely influenced earthquake recurrence and slip rate along the SVF.

ACKNOWLEDGEMENTS

I'd like to thank CWU School of Graduate Studies and Research for the Master's Research or Creative Activity award and the Summer Research Fellowship that funded my field work in summer 2015. Additional funding from a NEHRP grant allowed me to present my findings at the Fall AGU conference in 2015. I'd like thank my advisor Anne Egger for constantly pushing me to be better and guiding me along this process. I want to also thank the valuable advice and opinions of my colleagues, especially Dr. Johnathan Glen, for taking me into his home and giving me a crash course in 2D potential field modeling. Lastly, I would like to thank my fiancée Kimberly Edwards for all of the love and support that I could have ever wanted and keeping me (relatively) stress-free.

TABLE OF CONTENTS

LIST OF TABLES

LIST OF FIGURES

CHAPTER I

INTRODUCTION

The northwestern Basin and Range (NWBR, Figure 1, 2) is a region with numerous major normal faults that have no historical earthquakes along them. These normal faults are still interpreted as active however, indicated by the presence of fault scarps that cut Quaternary sediments (Personius et al., 2009; Personius et al., 2007; Pezzopane, 1993; Pezzopane and Weldon, 1993). These faults, including the Surprise Valley fault, Alvord fault, Winter Rim fault and Slide Mountain fault (Figure 1, 2), have Quaternary slip rates that range from 0.5 to 2 mm/yr and are known through paleoseismology, to have large estimated M6.8-7.3 earthquakes (Personius et al., 2009; Personius et al., 2007; Pezzopane, 1993; Weldon et al., 2013). Slip rates along faults are necessarily time-averaged, calculated by measuring the offset of a feature of known age, while earthquakes are discrete events during which slip actually occurs. As more fault offset, and time data is collected, we are better able to resolve the slip rate over time and connect it directly to earthquakes.

Pleistocene pluvial lakes in the NWBR filled valleys bounded by normal faults (Figure 2) and produced sets of datable paleoshorelines that provide time resolution in thousands of years. Paleoshorelines are ideal features to use in slip rate calculations, because they are basin-wide, paleohorizontal features that may cross faults and can be precisely dated. Carbonaceous tufa were deposited approximately contemporaneously with shoreline formation in this region and provide the basis for calculating slip rates along the faults.

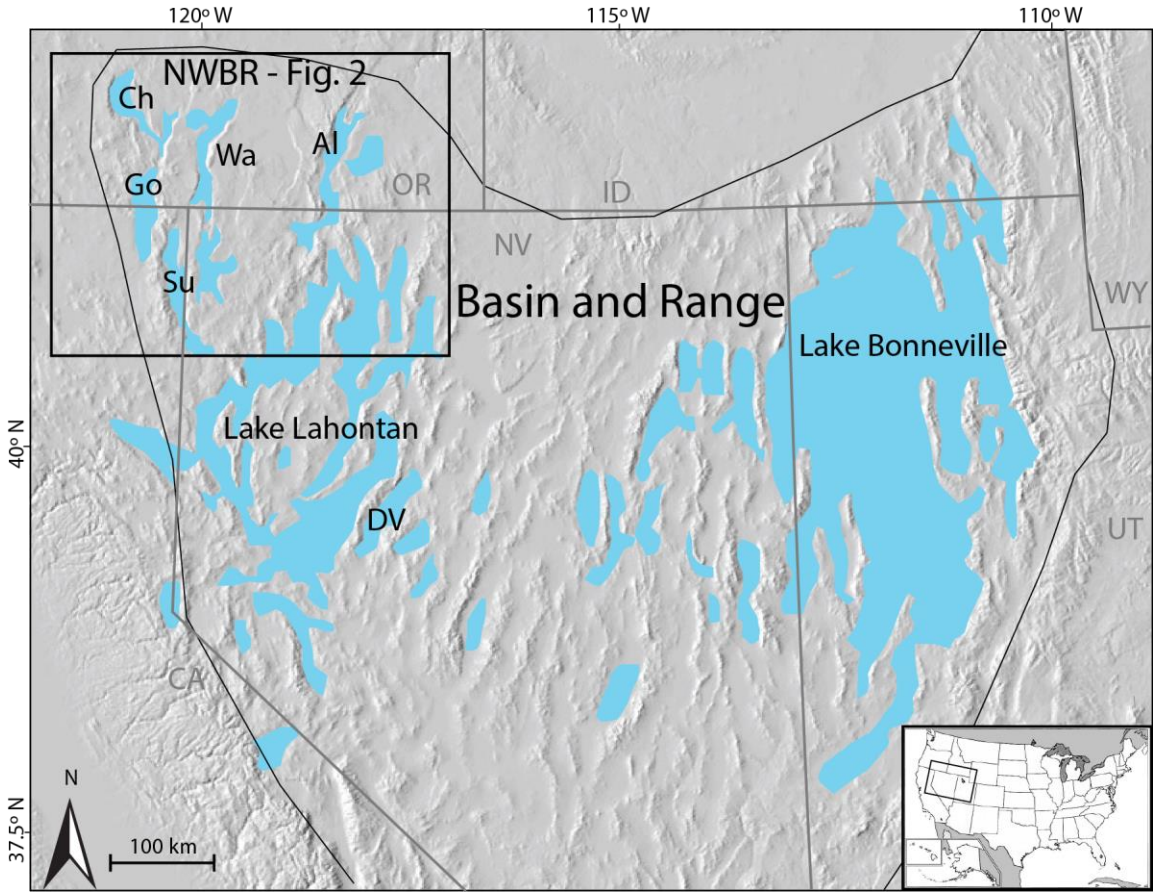

Figure 1. Overview map of the Basin and Range showing the distribution of lakes during the Late Pleistocene overlain on a shaded relief map. Major pluvial lakes in the NWBR: Ch - Lake Chewaucan; Go - Goose Lake; Su - Lake Surprise; Wa - Lake Warner; Al - Lake Alvord. Dixie Valley, NV labeled as DV.

Both the filling of reservoirs and recession of pluvial lakes have been shown to potentially induce earthquakes (Bell and Nur, 1978; Gupta, 2002; Weldon et al, 2009) and modify slip and slip rates (Oldow & Singleton, 2008; Karow and Hampel, 2010). Rapid changes in lake levels alter the state of stress through a combination of a change in the vertical stress, change in pore fluid pressure in saturated rocks, and raising of the water table, all of which can induce (or suppress) seismicity (Gupta, 2002). In the Summer Lake basin, for example, pre-historic earthquake cluster on the Ana River fault (Figure 2) correlates with rapid removal of Lake Chewaucan (Weldon et al, 2009), and

seismogenic landslides could have been facilitated by the heightened water table associated with the lake (Badger and Watters, 2004).

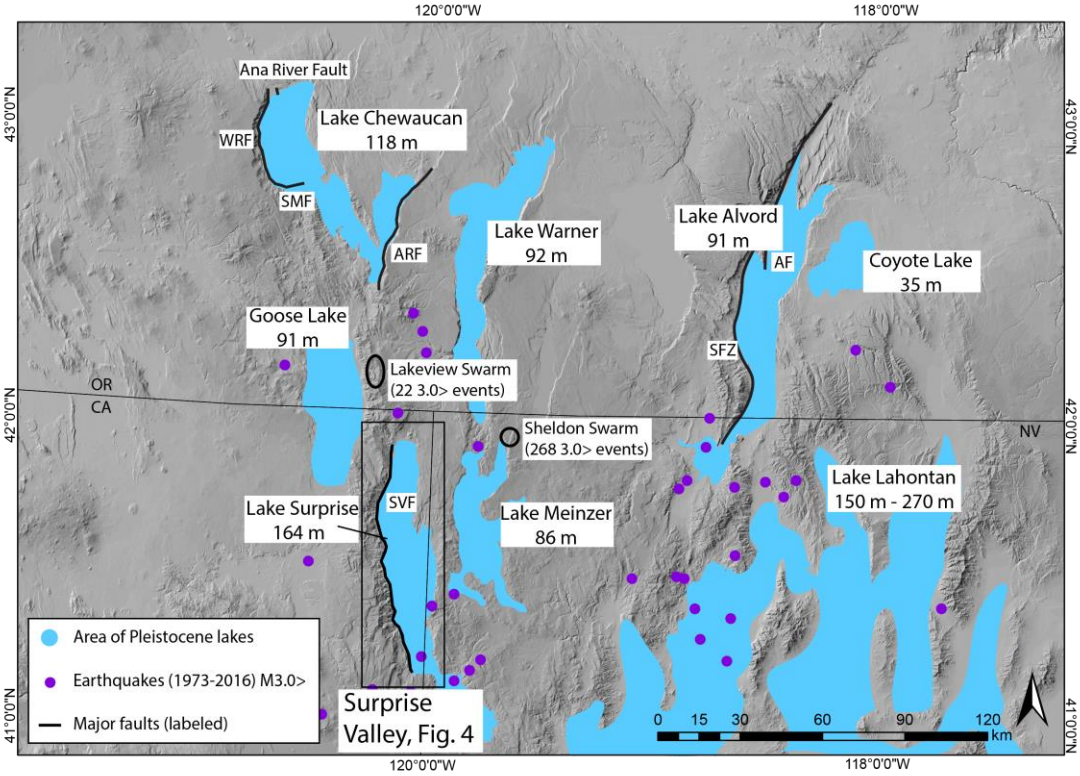

Figure 2. Shaded relief map of the northwestern Basin and Range province. Blue regions denote the maximum spatial extent of the many Pleistocene pluvial lakes that filled the fault controlled valleys (Ibarra et al., 2014; Reheis, 1999). Depths of the lakes are displayed in meters. Labeled major faults: SVF - Surprise Valley fault, WRF - Winter Rim fault, SMF - Slide Mountain Fault, ARF - Abert Rim Fault, AF - Alvord Fault, SFZ - Steens Fault Zone. The purple circles are locations of earthquakes over the last 43 years with a M3.0> in size (Provided by USGS from the ANSS Comprehensive Catalog)

Surprise Valley (Figure 2) is bound by the Surprise Valley fault (SVF), an active normal fault with at least five earthquakes of estimated M 6.8-7.3 since 35 ka and an irregular earthquake recurrence interval of 4.2 ± 4.7 ka (Personius et al., 2009). Surprise Valley also hosted a pluvial lake that reached its highstand ~15 ka. Additional dated paleoshorelines constrain the lake level history over the last 25 ky (Ibarra et al., 2014). These two datasets of earthquakes and paleolake levels, in combination with detailed

mapping afforded by high-resolution topographic data, allow us to address the following question: What role, if any, has pluvial Lake Surprise played on the spatial and temporal variations of slip along the SVF?

By mapping paleoshoreline features with high-resolution topographic data and obtaining radiocarbon dates on paleoshoreline tufas, I document precise offsets of dated features over the last 25 ka, refining the spatial and temporal variation of slip along scarps associated with the SVF. Potential field modeling of gravity and magnetic data along limited number of profiles suggest that the surficial scarps continue at depth, where they may accommodate greater offset. These results refine the time-averaged slip rate along the SVF and show variability both through time and along the length of the fault, allowing for correlations with paleolake level changes. This study suggest potential relation between pluvial lakes and their proximal faults that show the lake likely influenced earthquake recurrence and slip rate along the SVF.

CHAPTER II

BACKGROUND

Tectonic Setting

The northwestern Basin and Range (NWBR) spans California, Nevada, and Oregon (Figure 1). Normal faults in this region have been active since at least 12 Ma (Colgan et al., 2006; Henry and Perkins, 2001; Lerch et al., 2008). It is a low-strain region (Kreemer et al., 2012) that has accommodated only about 15% extension since 15 Ma (Egger and Miller, 2011).

Major normal faults that have accommodated that extension in this region include the Surprise Valley fault (Egger and Miller, 2011; Egger et al., 2009; Egger, 2014; Personius et al., 2009), Slide Mountain and Winter Ridge faults in the Chewaucan Basin (Personius, 2002; Pezzopane and Weldon, 1993; Pezzopane, 1993; Weldon et al., 2009); the Abert Rim Fault (Scarberry et al., 2010); and the Alvord and Steens faults in the Alvord basin (Personius et al., 2007; Oldow and Singleton, 2008) (Figure 2). Despite the low strain rate and lack of historical earthquakes, these faults have been shown to be capable of producing M>6.8 earthquakes during the Pleistocene (Personius et al., 2007, 2009) (Table 1). Table 1 contains a detailed list of the major normal fault-bound valleys and their associated Pleistocene pluvial lakes in the NWBR. All demonstrate a pluvial lake highstand within 12 to 15 ka, and have major normal faults with slip rates that range from 0.2-1.0 mm/yr. The most recent surface rupturing earthquake occurred in 1954 from the Dixie Valley EQ. Within the NWBR however, surface rupturing earthquakes have not occurred during the period of historical records (~150 years), with the most recent event

occurring along the SVF at 1.2 ± 0.1 ka. More recent seismicity (Figure 2) ranges from M1.0 - M5.0 throughout the region, mostly not along range-bounding normal faults, and in two swarms, the 2004 Lakeview Oregon swarm (26 M>3.0 events), and the ongoing Sheldon Swarm (268 M>3.0 events since 2014).

Table 1. Pluvial Lake and Fault Data

Pluvial lake	Age of lake highstand	Method to determine age	Major fault	Holocene Slip Rate	Most recent major EQ (M>7)
Lake Surprise	15 ka [1]	Radiocarbon tufa [1]	Surprise Valley fault	0.6 mm/yr [2]	1.2 ± 0.1 ka [2]
Lake Chewaucan	12 ka [3]	Radiocarbon tufa [3]	Slide Mountain fault Winter Rim fault	0.4-0.6 mm/yr; 0.5 mm/yr [4] 0.3-1.0 mm/yr [5]	2.1 - 15 ka [6,7] <15 ka [6]
Lake Alvord	13-14 ka [8]	Tephra dating [8]	Alvord fault	0.24 mm/yr [9]	4.6 ± 1 ka [9]
Lake Lahontan	13 ka [10]	Radiocarbon animal bones [10]	Various	Typically 0.1 - 0.55 mm/yr [11]	Dixie Valley EQ: 1954 AD

[1] Ibarra et al., 2014, [2] Personius et al., 2009, [3] Licciardi, 2001, [4] Weldon et al., 2013, [5] Pezzopane, 1993, [6] Personius, 2002, [7] Pezzopane and Weldon, 1993, [8] Carter et al., 2006, [9] Personius, 2007, [10] Adams and Wenousky, 1998, [11] Karow, 2009

The NWBR also hosted pluvial lakes over the last 2 My that filled normal-fault bound basins (Figure 2). These lakes on average lasted 25 ky with interpluvial periods lasting 40-60 ky (Negrini et al., 2000), leaving evidence of their existence in the form of both erosional and depositional geomorphic features formed during high-stands and still-stands (e.g. Reheis, 1999). Wave-cut terraces are the most prevalent feature and are exposed discontinuously around the basins (Figure 3). Carbonate tufa formed along these terraces within the photic zone and likely near the lake surface and edge (Felton et al., 2006), thus tufa elevations give minimum lake surface elevations at their time of deposition (Figure 3). Radiocarbon dating can be used to determine the age of tufa formation, and thus the tufas can be used as age markers for changes in lake level. Because paleoshorelines are paleo-horizontal features, any offset in elevation between

individual or sets of dated shorelines record deformation. This source of data provides a record of the interactions between fault displacement and lake-level changes.

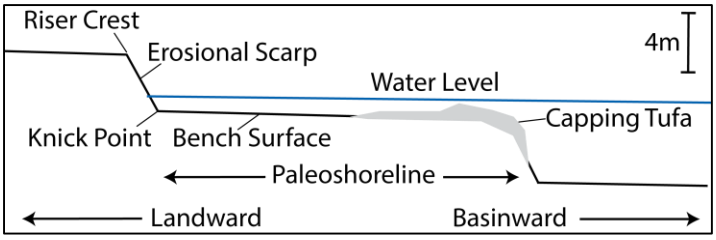

Figure 3. Schematic drawing of tufa locations on Provo shoreline benches. Tufa commonly occurs in patches on the outer edges of benches Modified from drawings contained in Felton et al., 2006 and Oldow and Singleton, 2008.

Connections Between Earthquakes and Lakes

Despite being relatively short-lived and spatially limited features, pluvial lakes have profound effects on the landscape and tectonics of a region. These effects include flexure of the crust as the lake level rises and isostatic rebound as the lake recedes (e.g. Gilbert, 1890), facilitation of large landslides (e.g. Badger and Watters, 2006), and the suppression or enhancement of earthquakes and slip rate (e.g. Karow and Hampel, 2010; Hampel et al., 2010).

Flexure and isostatic rebound

Large lakes produce deformation through crustal flexure, as first noted by Gilbert (1890) in the Bonneville basin (Figure 1). He documented that the shorelines in the Bonneville basin had changed in elevation since their formation and that this phenomenon could not be attributed to faulting. This idea of crustal flexure was refined and built upon by several workers, including Crittenden (1963) and Nakiboglu and Lambeck (1983), who modeled deformation of the crust comprising an elastic layer overlying a viscoelastic channel. Their results showed that the lithosphere of the

Bonneville basin was 28-30 km thick and rates of present isostatic uplift ranged from 0.03 mm/yr at the fringes to 0.06 mm/yr at the center of the basin (Nakiboglu and Lambeck, 1983).

Crustal flexure is documented in the Lahontan basin (Figure 1) as well. At the margins of the basin, constructional beach bars on the east side of Dixie Valley show eastward tilt of 0.16 m/km, mirroring the westward tilt of similar features on the west side of the Lahontan basin, indicating that lithospheric rebound was symmetrical with a magnitude of 22 m at its greatest (Caskey and Ramelli, 2004).

Simple 2D models of flexural response of the crust to loading by the Lake Surprise highstand were developed (Figure 4, Egger and Ibarra, 2012). In both E-W and N-S profiles, the maximum flexure is at the center of the lake, but both models assume blocks of infinite length in the third dimension. For a deep, narrow lake, the E-W model is likely closer to the real flexure that occurred during the Last Glacial Maximum, but it is still almost certainly a significant overestimate (Egger and Ibarra, 2012). In addition, the effect of flexure in the Surprise Valley basin would be symmetrical across the basin, so any relative change in elevation across the valley would not be from isostatic rebound and could be attributed to faulting.

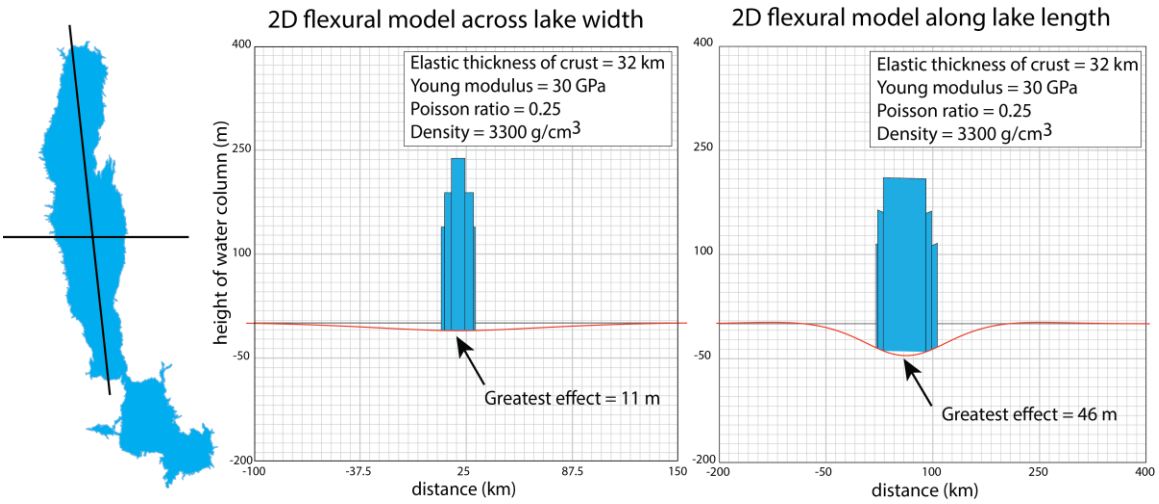

Figure 4. 2D models of the flexural response of the crust to loading by the lake highstand using OSXFlex2D Version 3.3 written by Allmendinger and Cardozo (Egger and Ibarra, 2012). Two models were constructed: one running approximately E-W across the lake, and the other approximately N-S. These models provide an absolute maximum for the effect of isostatic rebound could have on the current elevations of paleoshorelines (Egger and Ibarra, 2012)

Lake Bonneville at its maximum covered 52,000 km^2 and was over 300 m deep (Karow and Hampel, 2010); Lake Lahonton covered ~22,000 km^2 and had a depth of ~200 m (Karow and Hampel, 2010). In comparison, Lake Surprise covered 1366 km^2 with a depth of 176 m (Ibarra et al., 2014). The weight of the water that filled Surprise Valley is significantly less than the water that filled the Bonneville and Lahontan basins (Figure 4, Hampel et al., 2010; Karow and Hampel, 2010), and thus the amount of crustal flexure and isostatic rebound is negligible for this study.

Earthquake triggering

In addition to causing flexural deformation of the crust, lakes can either enhance or suppress earthquakes by increasing the elastic stress, decreasing pore volume and increasing pore fluid pressure in underlying sediments, raising the water table, and lubricating fault zones (Bell and Nur, 1978). The triggering of earthquakes by filling of

artificial reservoirs has been known for over 70 years (Gupta, 2002). Koyna, India continues to be the most significant site of earthquakes triggered by a water reservoir behind a human-constructed dam. During 1990s, two events exceeding M 5 and several smaller events occurred near the then-recently impounded Warna Reservoir (Gupta, 2002). In more recent years, the M 7.9 2008 Wenchaun Earthquake in China may have been triggered by the mass loading and increased pore pressure caused by the impoundment of the Zipingpu reservoir (maximum depth of 121 m) (Xiao, 2012).

Fewer studies have addressed the effect of the *removal* of lakes on seismicity, though recent modeling has begun to do so (e.g. Karow and Hampel, 2010; Hampel et al., 2010). The impoundment and recession cycle of a single pluvial lake act on timescales on the order of 10^4 yrs (Licciardi, 2001). Artificial reservoirs in comparison are shorter-lived, lasting up to ~100 yrs (Gupta, 2002). Extensional tectonic environments, the NWBR specifically, can last up to 10^6 yrs, outlasting the pluvial features (Colgan et al., 2008). The SVF formed on the order of 14 Ma and has shown to have an average slip rate of 0.5-0.6 mm/yr over that time period (Egger and Miller, 2011; Lerch et al., 2008).

Colgan et al. (2008) have shown exhumation rates of a granitic, conglomerate clast likely varied. This work suggests that the tectonic stress environment has been approximately constant on the order of 12 Ma since the initiation of the SVF. (Egger and Miller, 2011; Colgan et al., 2008). The recession of pluvial lakes potentially affects short term seismicity (on timescales of 10^4 yrs) through changes in stress regime, pore pressure, water table elevation, and fault lubrication (Gupta, 2002). Examples of these effects can be seen within the Chewaucan basin, the Alvord basin, and the Lahontan and

Bonneville basins during the late Pleistocene (Weldon, 2009; Weldon et al., 2013; Oldow and Singleton, 2008; Karow and Hampel, 2010).

Paleoseismic trenching across the Ana River fault in the Chewaucan Basin (Figure 2) reveals evidence for 10 paleo-earthquakes into deep-water lacustrine deposits that contain 50 dated volcanic ashes (Weldon et al., 2013). Of these events, there is a documented cluster of three M7.0 earthquakes in the past 7-13 ka, during Lake Chewaucan recession. The tight clustering of these earthquakes is three times the number expected from the average recurrence interval over the previous 70 ka when the fault was under the lake (Weldon et al., 2009).

In the Alvord Basin (Figure 2), active normal faults disrupt sets of shorelines of pluvial Lake Alvord that formed during at least two periods of lake-level highstands in the Pleistocene (Oldow and Singleton, 2008). Variation in shoreline spacing measured across 8 faults in the region and on opposing sides of the basin indicates that a greater percentage of total fault slip occurred during and following lake-level recession. Displacement rates estimated over 10^4 yr exceed geodetic rates by two to three times and are greater than rates estimated over 10^5 yr by a factor of five or ten (Oldow and Singleton, 2008). This analysis of shoreline offset doesn't directly indicate timing of earthquakes, but suggests that slip and slip rates changed with the impoundment of the pluvial lake.

These field-based studies of single basins are complemented by modeling studies. Hampel and Hetzel (2006) developed a finite element model to evaluate how the magnitude, distribution, and temporal evolution of a load, influence normal faults. They

calculate the load of both a large lake and glacial ice to model how the rate of faulting on normal faults may be controlled by large mass fluctuations on the surface. They show that there is a duration of time during loading that is seismically quiet and then during unloading, a slip rate increase that are primarily controlled by the weight and spatial distribution of the load. Asthenosphere viscosity imparts a time lag between loading and the slip rate decrease along the fault as well as a time lag between unloading and the corresponding slip rate increase. Factors that play only a minor part in a fault's response include thickness of the lithosphere, fault strength, and the rate of load removal (Hampel and Hetzel, 2006).

The location of the fault with respect to the greatest load of the lake also appears to be a dominant parameter that affects variations of slip rate along the fault. In more refined models of Lake Bonneville and Lake Lahontan that take into account the location of the faults, rheological parameters of the lithosphere, and temporal evolution of maximum water depth, Karow and Hampel (2010) distinguished two patterns of slip rate variation, based on where the fault is located relative to the load of the lake. Normal faults near the center of the lake responded to loading by a decrease in slip rate and to unloading by an increase in slip rate. In contrast, normal faults located along the periphery of the lake increase in slip rate during loading and decrease during unloading (Karow and Hampel, 2010).

Inducement of large landslides

Within the NWBR, the presence of the pluvial lakes can raise the water table and saturate sediments that fill the valleys. This saturation exerts an outward force on the top soil in the form of pore pressure and an increased weight that can weaken slopes and create instability. In the Summer Lake basin (Figure 2), gigantic landslides, 4.4 km^3 in volume total, line the southwestern part of the Winter Rim (Badger and Watters, 2004). One landslide in particular, the Punchbowl landslide, has neopluvial shorelines dated between 4 and 1.9 ka and no older Pleistocene shorelines, constraining the event to just after the Pleistocene pluvial episode at 10 ka (Badger and Watters, 2004). Two other landslides, the Bennett Flat and the Foster Creek landslides have minimum age constraints during the Pleistocene pluvial highstand at 13–16.8 ka (Badger and Watters, 2004; Licciardi, 2001; Negrini and Davis, 2002). The landslides initiated along planar failure surfaces dipping 5° E within weak tuffaceous sedimentary rocks, which are stable under static conditions. Badger and Watters (2004) modeled conditions at failure under a variety of parameters that included groundwater content, slopes, stratigraphy and derived shear strength. The model results suggest that strong shaking was required to trigger the landslides (Badger and Watters, 2004). Landslides within the Winter Ridge system met nearly all of the criteria for earthquake-induced landslides proposed by Crozier (1992).

The largest fault within the NWBR and the target fault of this study is the Surprise Valley Fault (Figure 2, 5). Today, we have access to the paleoseismology of the fault from trench logs, as well as a robust hydrograph for the pluvial Lake Surprise. This

combination of data provides the best starting point for examining the relationship between earthquakes and lakes.

Surprise Valley

Surprise Valley is a N-S trending valley approximately 90 km long (Figures 2, 5). It is bounded by the SVF and the Warner Range to the west, and the smaller Hays Canyon fault and Hays Canyon Range to the east (Egger and Miller, 2011) (Figure 5). Playas in the northern, central and southern sub-basins occupy the valley floor (Figure 5). The basin is estimated to be filled with 1-2 km of Tertiary and Quaternary sediments (Lerch et al., 2009). Numerous fault scarps line the western side of the valley (Figure 5). These were initially mapped by Hedel (1980); Bryant (1990) reevaluated this initial effort and removed several features determined to be paleoshoreline features. Egger (2014) refined this scarp map further using high-resolution lidar data.

Paleoseismic trenching along the SVF reveals at least 5 earthquakes M 6.8–7.3 in the last 35 ka, with a recurrence interval of 4.2 ± 4.7 ka and a late Holocene slip rate of 0.6 ± 0.1 mm/yr (Personius et al., 2009). The most recent earthquake is presumed to be recorded in scarps in active alluvial fans and are present in ~42 km of the SVF (Egger, 2014). Estimates of the magnitude from point measurements of surface rupturing of this event are M7.0-7.3 (Egger, 2014), which agrees well with the estimates from paleoseismic trenching.

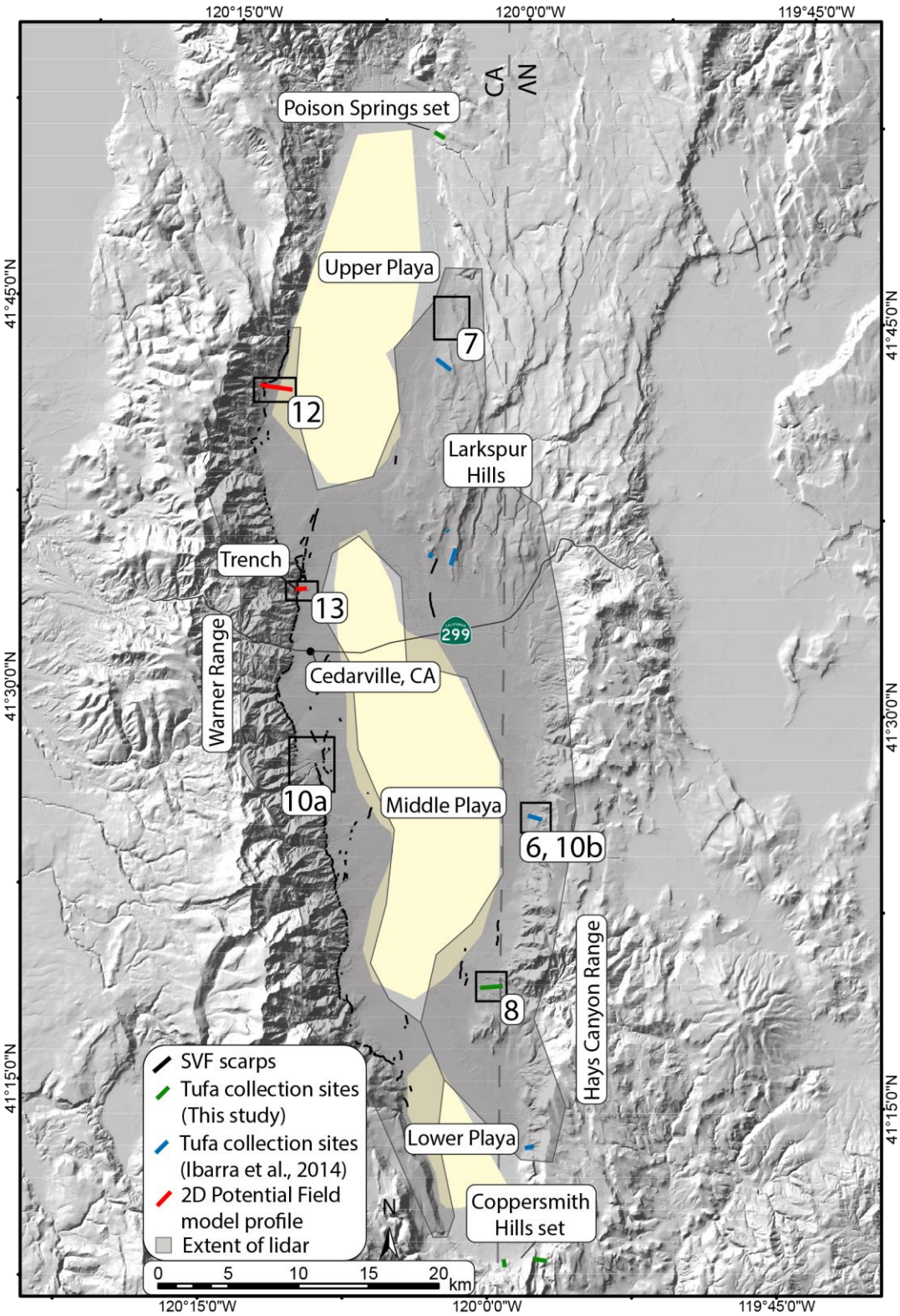

Figure 5. Shaded relief map of Surprise Valley. Black boxes mark the location for figures later in this paper.

Seismic reflection profiling demonstrates that the SVF dips at a moderate angle, only ~30°, to ~2 km depth (Lerch et al., 2009). Based on a detailed magnetic and gravity profile, Egger et al. (2009) identified several faults within the valley that may accommodate hundreds of meters of vertical offset. These faults possibly are cutting and offsetting the ~30° east-dipping Surprise Valley fault that was rotated during footwall tilting of the Warner Mountains. Some of these intra-basin faults correspond with mapped fault scarps, but others do not have surface expressions (Egger et al., 2009). A 200 m-long shallow seismic reflection profile near Cook's Canyon across the exposed fault scarp suggests that, to a depth of ~175 m, the SVF is steeply dipping at ~50-60° (Kell-Hills et al., 2008).

Along the eastern side of Surprise Valley, shoreline features are eroded into bedrock and Quaternary deposits (Figure 6). Laminated shoreline tufa on exposed bedrock and as laterally continuous gravel deposits are abundant on most shorelines between 1410 m and 1545 m (Figure 6). Several tufa deposits on these shorelines have been dated: the oldest dated shoreline is at an elevation of 1419.5 m and dates to 22.13 ± 0.23 ka, while the lake highstand at 1531 m dates to 15.19 ± 0.18 ka (Ibarra et al., 2014). Dated paleoshorelines span all three sub-basins of the Surprise Valley (Figure 5).

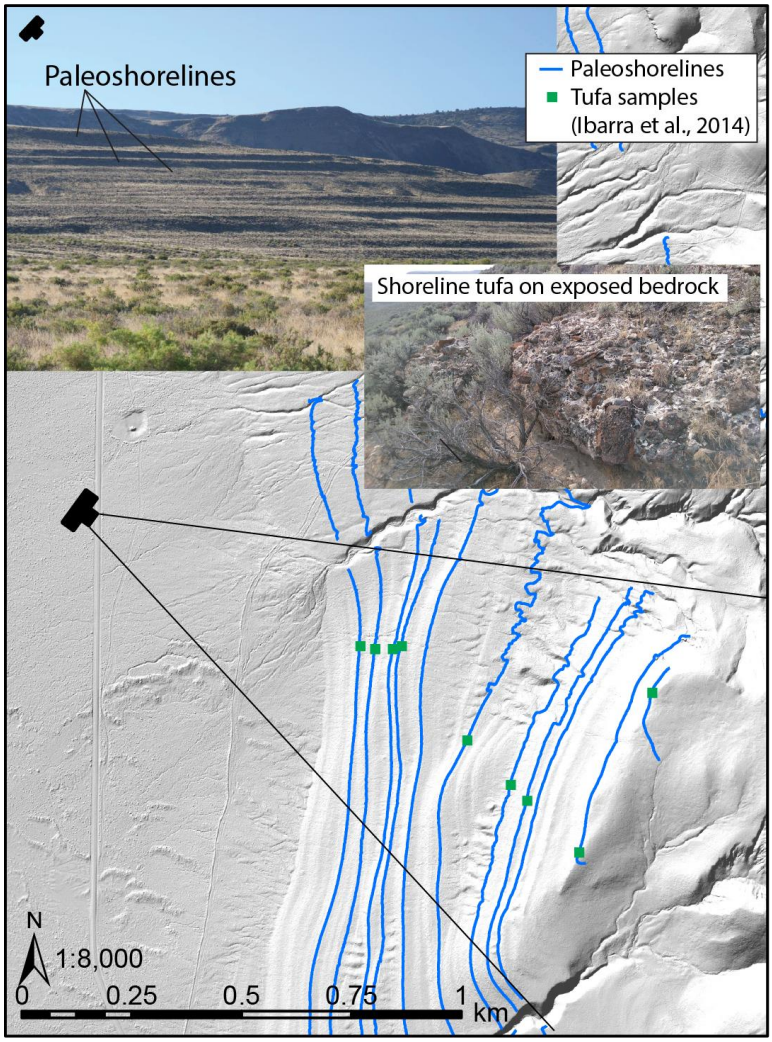

Figure 6. Clockwise from the top: picture of a paleoshoreline outcrop in the field; picture of shoreline tufa on exposed bedrock. Hillshaded digital elevation model showing the location of the top picture.

Regional gravity and magnetic data along with several detailed transects are available for Surprise Valley (Ponce et al., 2009). Many studies have utilized this data to access geothermal potential and to map subsurface structures within the basin (Egger et al., 2009; Lerch et al., 2006; Glen et al., 2008). Rock properties are well measured and defined for the region, which helps in potential field modeling (Benoit et al., 2005; Ponce et al., 2009).

The new mapping, geochronology, and analysis of shoreline offset, coupled with potential field modeling presented in this study allow us to build a more comprehensive history of the Surprise Valley fault and how slip along the fault is related to pluvial Lake Surprise.

CHAPTER III

METHODS

Lidar-Based Mapping and Paleoshoreline Offset

I mapped paleoshorelines and fault scarps on hillshade and slope maps derived from lidar data acquired by the National Center for Airborne Laser Mapping (NCALM) (Figure 5). I first focused along the western side of the valley, where the shorelines are less pronounced and not as laterally continuous as the eastern side of the valley. Using a slope map draped over a shaded relief map, I identified alternating patterns of shallow (0-6° benches) to steeper slopes (>10° erosional scarps) that form the paleoshoreline (Figures 3, 7) (Reheis et al., 2014). The line intersecting the bench and erosional scarp represents the riser crest of a wave-cut terrace (Figure 3) and was drawn in by hand. These were typically in sets of three or more parallel shorelines. Along the eastern side, I identified paleoshorelines by generating contour lines at elevations of known, dated shorelines from field mapping (Ibarra et al., 2014) and then removed sections of the contour lines that did not match observable geomorphic features.

I had specific criteria for mapping shorelines along the eastern edge of the valley. Shorelines were mapped along elevations that have had tufa collected from and dated through radiocarbon. In addition, the shorelines were mapped in three sections, northern, central, and southern. Shorelines mapped in the northern section matched with tufa that was dated in the same section. When tufa was gathered at the same elevation within error in multiple sections, the shoreline was mapped through every section. These criteria were imposed to emphasize dated shorelines. Using the lidar-derived DEM, I measured

vertical spacing between individual shorelines and sets of shorelines along the eastern and western sides of the valley in ArcGIS.

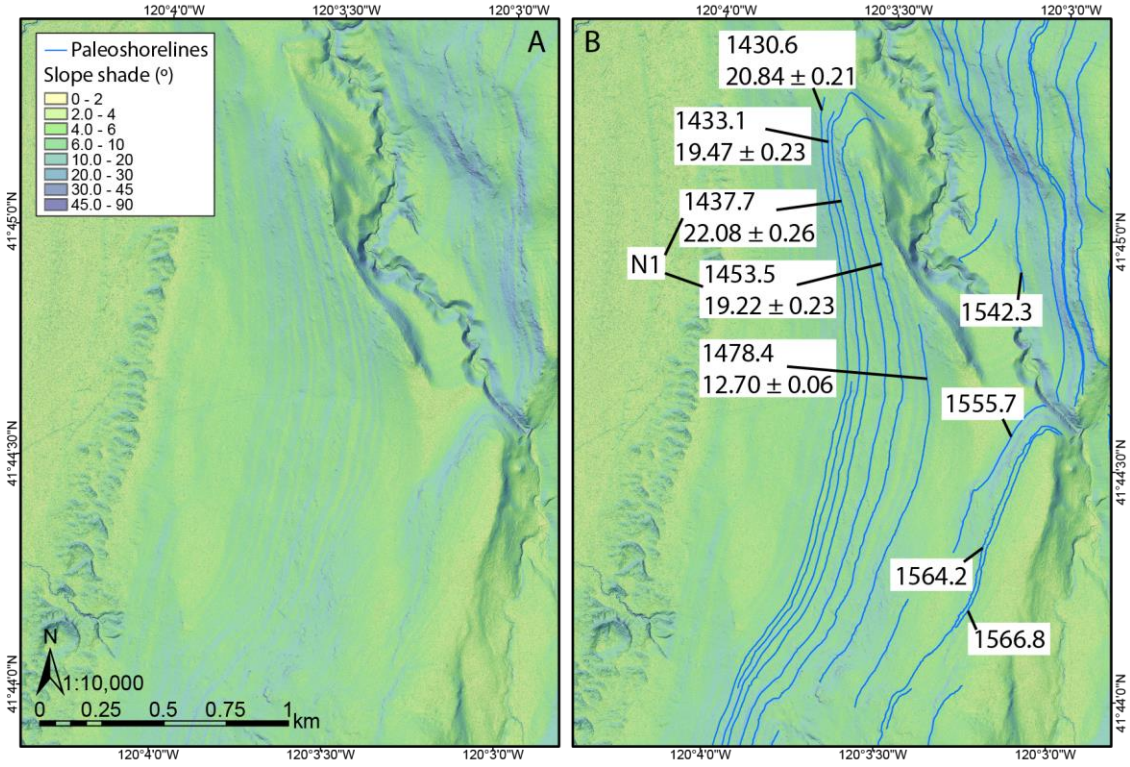

Figure 7. A) Slopeshade draped over a hillshaded digital elevation model. The varying green to blue colors indicate patterns of shallow to steeper slopes that can be mapped. B**)** Interpreted paleoshorelines drawn onto the DEM. Note, only paleoshorelines at elevations that tufa has been collected and dated have been mapped. Refer to box labeled 7 in Figure 5 for location.

A shoreline set consists of two or more shorelines with consistent differences in elevation in all locations where the shorelines are expressed, even though the absolute elevation may differ (such as on opposite sides of the valley).

Assessing paleoshoreline offset in each section shows how the offset differs along strike. I correlated sets of shorelines along the eastern and western sides of the valley by looking for similar vertical spacing, and then measured the difference in the absolute elevation of the sets in ArcGIS.

Radiocarbon Dating

Twenty-six samples from three localities were collected in August 2015 from laterally continuous tufa deposits on beach gravels and exposed bedrock on the front edge of the crest of horizontal shoreline benches, and wave-cut terraces (Figure 8). The sample localities were targeted to fill the spatial gaps in the data from previous studies (Ibarra et al., 2014) in the northern and southern-most reaches of the valley (Figure 5). Latitude and longitude of sample locations were recorded with a handheld GPS (Garmin eTrex 20). Sample elevations were determined by pinning the location coordinates to the lidar-derived DEM where possible, reducing the uncertainty in the elevation of the samples to ± 0.1 m.

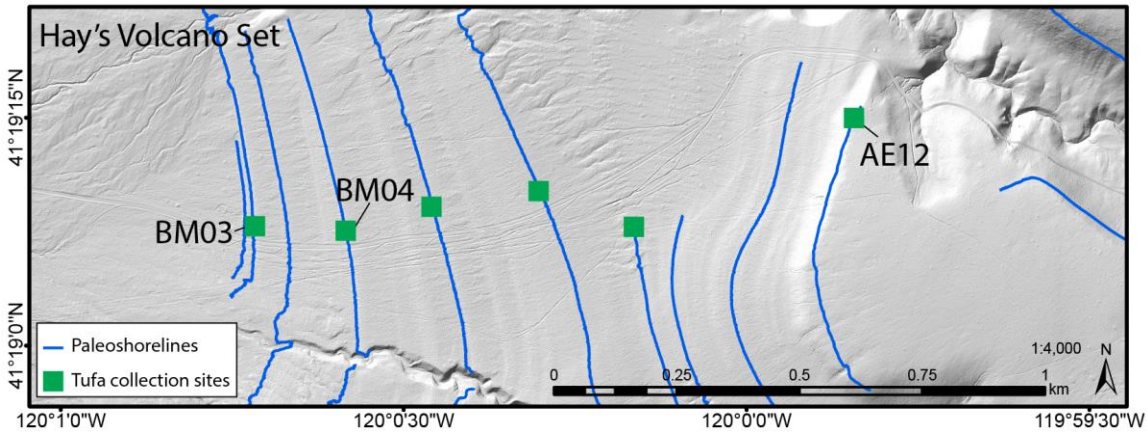

Figure 8. Location map for samples in the Hay's Volcano set collected as part of this study. Sample locations (latitude, longitude, and elevation) are listed in Table 2. These were plotted on a hillshaded digital elevation model. The locations of the Poison Springs and Coppersmith Hills sets are shown in Figure 5.

Ten of the samples were selected for radiocarbon dating on the basis of (1) the density of carbonate, selecting samples that had few vesicles; (2) sample size, large enough to be handled and small enough to meet the weight criteria for shelly carbonates, and (3) clearly laterally continuous and in situ in the three target areas. Each sample was

put through an ethanol wash to clear off any foreign carbon acquired during the collection process. Samples were carved into 30 mg chunks of dense carbonate using a dremel with a reinforced-steel rotary saw blade. In cases where the tufa was thick and laminar, all sides of the tufa were shaved until a vesicle-free core of the tufa remained.

The samples were sent to DirectAMS Radiocarbon Dating Services in Bothell, WA, and processed according to their protocols (http://www.directams.net/Services-and-Fees.html). I received uncalibrated ages, and calibrated them using the Calib 7.0 program with IntCal13 (Stuiver and Reimer, 2005; Reimer et al., 2013).

Geophysical Modeling

The magnetic and gravity data I utilized was collected to investigate the geothermal systems at depth within the basin (Egger et al., 2009; Ponce et al., 2009). I modeled two profiles that were pulled from detailed gravity and magnetic data that crossed mapped SVF scarps. Because the data were not always collected in straight lines across the SVF, the data were gridded and straight-line profiles were drawn across the SVF along the grids to develop two-dimensional (2D) potential field models using a 2D forward modeling package (GMSYS®). The gravity and magnetic anomaly data were gridded to a minimum curvature surface similar to that described by Briggs (1974) and Swain (1976). This gridding process was utilized due to being able to apply linear gridding and work with any spatial distribution of data. Minimum curvature gridding outputs grids up to any size, which enabled me to draw a best-fit profile line through the gravity and magnetic gridded data for the 2D potential field models.

These methods closely follow those from Egger, Glen, and Ponce (2009), but are summarized here. The models incorporate information from geologic mapping (Egger and Miller, 2011), seismic reflection (Lerch et al., 2009), wells and drill-cores (Benoit et al., 2005; Miller et al., 2005), and measured rock-property data (Ponce et al., 2009). For sedimentary deposits in the basin, I used P-wave velocity-derived densities for subsurface units in the basin (Egger et al., 2009, constrained by hand samples taken in the area (Ponce et al., 2009) and drill-core data (Miller et al., 2005). Raw gravity data were reduced using standard gravity methods that include: free air, latitude, earth-tide, instrument drift, simple Bouguer, terrain, curvature, and isostatic corrections (Blakely, 1995) to yield isostatic anomalies. The gravity map and profile derived from these data reflect anomalies produced by lateral variations in crustal density.

Remnant components of magnetization directions of the model blocks were assumed to be parallel to a time-averaged geocentric axial dipole field direction with an inclination of 61° and declination of 0° (or inclination of -61°, and declination of 180°, in the case of reversely magnetized units). Magnetizations were assumed for units based on appropriate published values for rock types in the area (Ponce et al., 2009). The data were corrected for the diurnal variations, and filtered to remove cultural noise such as fences, passing cars, power lines, and culverts (Ponce et al., 2009). The map and profile derived from these data reflect magnetic field variations that arise mainly from contrasts in rock magnetic properties attributable to a number of different causes including depths to the magnetic sources, geothermal alteration, crustal structures juxtaposing different rock

types, variations in the concentration and type of magnetic minerals, and variations in remnant magnetization within rock units.

CHAPTER IV

RESULTS

Lidar Mapping and Radiocarbon Dating

Locations and elevations are given in Table 2, and the calibrated radiocarbon ages are provided in Table 3. An updated hydrograph of Lake Surprise with these new radiocarbon ages is provided in Figure 9. The ages of tufa all fall within the most recent cycle of Lake Surprise since the LGM. Shoreline elevations that we sampled in the northern lake basin match up with the same elevation shoreline in the southern lake basin within error: for example, SV15AE05 and SV15BM08 are on opposite ends of the valley, but share the same age (21.43 ± 0.26 ka and 21.46 ± 0.27 ka) and elevation (1443 ± 1 m and 1441 ± 1 m) within error. SV15AE12 provides an updated highstand of 15.98 ± 0.19 ka for Lake Surprise at an elevation of 1545.0 ± 0.1 m (Figure 9; Table 3). There are alternating periods of filling and receding lake water that includes a sharp drop in lake level right before the last highstand between 17 and 22.5 ka (Figure 9). The gradual filling of pluvial lakes has been assumed to be constant within Lake Bonneville (Oviatt et al, 1992), and with this new data, we can see that for Lake Surprise, there are distinct spikes of lake level recession, as has also been documented in Lake Lahontan (Broecker et al., 2009).

Table 2. Tufa Locations

Sample name	Latitude (°N)	Longitude (°W)	Elevation[a] (m)
Poison Springs set			
SV15AE01	**41.8608**	**120.07464**	**1462**
SV15AE02	**41.8612**	**120.07488**	**1470**
SV15AE03	**41.8616**	**120.07452**	**1491**
SV15AE04	41.86179	120.07451	1494
SV15AE05	**41.8611**	**120.07574**	**1443**
SV15AE06	**41.8624**	**120.07695**	**1437**
SV15AE07	41.8629	120.07728	1429
Hays Volcano set			
SV15BM03	**41.3190**	**120.01203**	**1440.2**
SV15BM04	**41.3189**	**120.00957**	**1458.5**
SV15BM05	41.31932	120.00834	1468.6
SV15BM06	41.31945	120.00669	1479.2
SV15BM07	41.31975	120.00520	1495.0
SV15AE12	**41.3213**	**119.99765**	**1545.0**
Coppersmith Hills set			
SV15BM01	41.14631	119.95898	1438
SV15BM02	41.14682	119.96005	1456
SV15BM08	**41.1445**	**119.98698**	**1441**
SV15BM09	**41.144**	**119.9865**	**1456**
SV15AE08	41.14667	119.95456	1384
SV15AE09	41.14514	119.95191	1445
SV15AE10	41.14455	119.95176	1482
SV15AE11	41.14588	119.94881	1497

[a]Poison Springs set and Coppersmith Hills set elevations were averaged from GPS elevations and 5 m pixel DEM
Sample names in bold were selected for radiocarbon dating

Figure 9 also includes a graphical representation of the timing of the five most recent large earthquake events as documented in Personius et al. (2009). The main clustering of earthquakes (P2, P3, and P4) appear to take place during the relatively quick period of drainage of Lake Surprise between 5 and 12.5 ka.

Table 3. New Radiocarbon Ages for Lake Surprise

Sample name	Laboratory Number	Latitude (°N)	Longitude (°W)	Altitude[a] (m)	^{14}C age (yr) ± 1σ	Calibrated age range (yr cal. BP)*,† ± 2σ	Median Age (yr cal BP)†,§	Calibrated age (ka cal. BP)*,† ± 2σ IntCal13
Poison Springs set								
SV15AE01	D-AMS 012850	41.8608	120.07464	1462	15551 ± 62	18663 - 18936	18808	18.80 ± 0.14
SV15AE02	D-AMS 012851	41.8612	120.07488	1470	14858 ± 56	17890 - 18259	18065	18.07 ± 0.18
SV15AE03	D-AMS 012843	41.8616	120.07452	1491	12089 ± 46	13786 - 14104	13956	13.95 ± 0.16
SV15AE05[b]	D-AMS 012844	41.8611	120.07574	1443[b]	17703 ± 59	21166 - 21690	21430	21.43 ± 0.26
SV15AE06	D-AMS 012845	41.8624	120.07695	1437	18201 ± 97	21815 - 22342	22069	22.08 ± 0.26
Hays Volcano set								
SV15BM03	D-AMS 012846	41.3190	120.01203	1440.2	14129 ± 60	16976 - 17439	17198	17.21 ± 0.23
SV15BM04	D-AMS 012847	41.3189	120.00957	1458.5	16199 ± 60	19338 - 19779	19556	19.56 ± 0.22
SV15AE12	D-AMS 012852	41.3213	119.99765	1545.0	13290 ± 46	15786 - 16167	15983	15.98 ± 0.19
Coppersmith Hills set								
SV15BM0[b]	D-AMS 012848	41.1445	119.98698	1441[b]	17725 ± 65	21192 - 21732	21461	21.46 ± 0.27
SV15BM09	D-AMS 012849	41.144	119.9865	1456	16427 ± 62	19606 - 20032	19821	19.82 ± 0.21

[a]Poison Springs set and Coppersmith Hills set elevations were averaged from GPS elevations and 5 m pixel DEM

[b]These shorelines are interpreted to be the same

* Calibrated using the Calib 7.0 program with IntCal13 (Stuiver and Reimer, 1993; Reimer et al., 2013).

† BP stands for "Before Present" where the "Present" is defined as the year 1950 A.D.

§ Median age calculated using the Calib 7.0 program

Paleoshorelines were mapped between 1400 m and 1550 m elevation (see Plate 1 in Appendix A). The shorelines were most easily mapped along the eastern side of the valley, and were most continuous between 1420 m and 1480 m elevation. Erosion to the shorelines at these elevations was largely due to wash out and sedimentation from alluvial fans coming off of the Hays Canyon Range. Vertical spacing between shorelines varied between 3 and 12 m (Table 4). All are late Pleistocene in age, from the latest

impoundment of Lake Surprise since the last glacial maximum (LGM) at 25 ka (Table 3) (Ibarra et al., 2014).

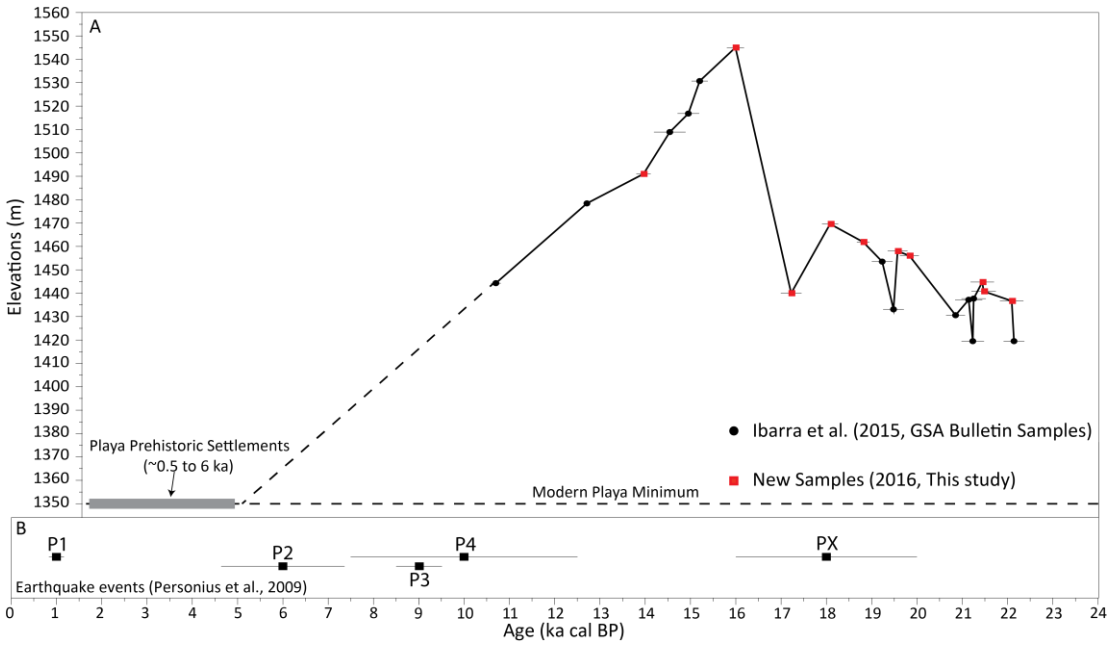

Figure 9. A) Lake Surprise shoreline elevation change graph. Sample ages calculated from 14C AMS dating. Dashed lines are tentative correlations. B) Timing constraints on prehistoric surface-rupturing earthquakes on the Surprise Valley fault from Personius et al. (2009). All ages are from the Cooks Canyon trench. The extent of the paleoseismic data extends back to 35 ka, the earliest earthquake event (PX) however, doesn't happen until 17-20 ka (Personius et al., 2009).

Paleoshoreline Offset

In the northern lake basin, I measured offset across the basin using paleoshoreline set N1 (Table 4). Paleoshorelines in the northern lake basin are offset by 4.3 ± 0.4 and 4.5 ± 0.4 m (Table 5). The central lake basin, I measured an offset of the paleoshoreline set N1 of 6.6 ± 0.7 m. and of paleoshoreline set C1 of 14.4 ± 1 m (Table 5, Figures 10, 11). In the southern lake basin, I measured vertical offset of shoreline sets S1 and S2 between 3.6 ± 0.2 to 5.5 ± 0.5 m (Table 5, Figure 11). Calculating slip from vertical offset measurements was done at three fault dips: 60° to represent standard normal fault mechanics (Anderson, 1951), 68° to match the dip of the fault in the trench (Personius et

al., 2009), and 35°, which is the modeled dip of the fault at depth from seismic reflection profile (Lerch et al., 2009).

Table 4. Shoreline Set Data

Shoreline set	Elevation (m)	Tufa sample name [1, 2]	Radiocarbon age (ka)
Northern Lake Section			
N1	1437.7	SV15AE06[1]	22.08 ± 0.26
N1	1453.5	SVDI11-T2[2]	19.22 ± 0.23
Center Lake Section			
C1	1508.9[a]	SVDI12-T9[2]	14.53 ± 0.35
C1	1516.8[b]	SVDI12-T10[2]	14.94 ± 0.24
Southern Lake Section			
S1	1427.8	SVDI12-T3[2]	-[3]
S1	1437.2	SVDI12-T13[2]	21.13 ± 0.30
S1	1440.2	SV15BM03[1]	17.21 ± 0.23
S2	1508.9[a]	SVDI12-T9[2]	14.53 ± 0.35
S2	1516.8[b]	SVDI12-T10[2]	14.94 ± 0.24
S2	1530.7	SVDI12-T14[2]	15.19 ± 0.18

[1]Tufa sample collected from this study
[2]Tufa sample collected from Ibarra et al. (2014)
[3]No radiocarbon age available for shoreline and tufa sample
[a] These shorelines are at the same elevation, and assumed to be the same age
[b] These shorelines are at the same elevation, and assumed to be the same age
Larger table that includes all shorelines mapped included in the appendix Table B1.

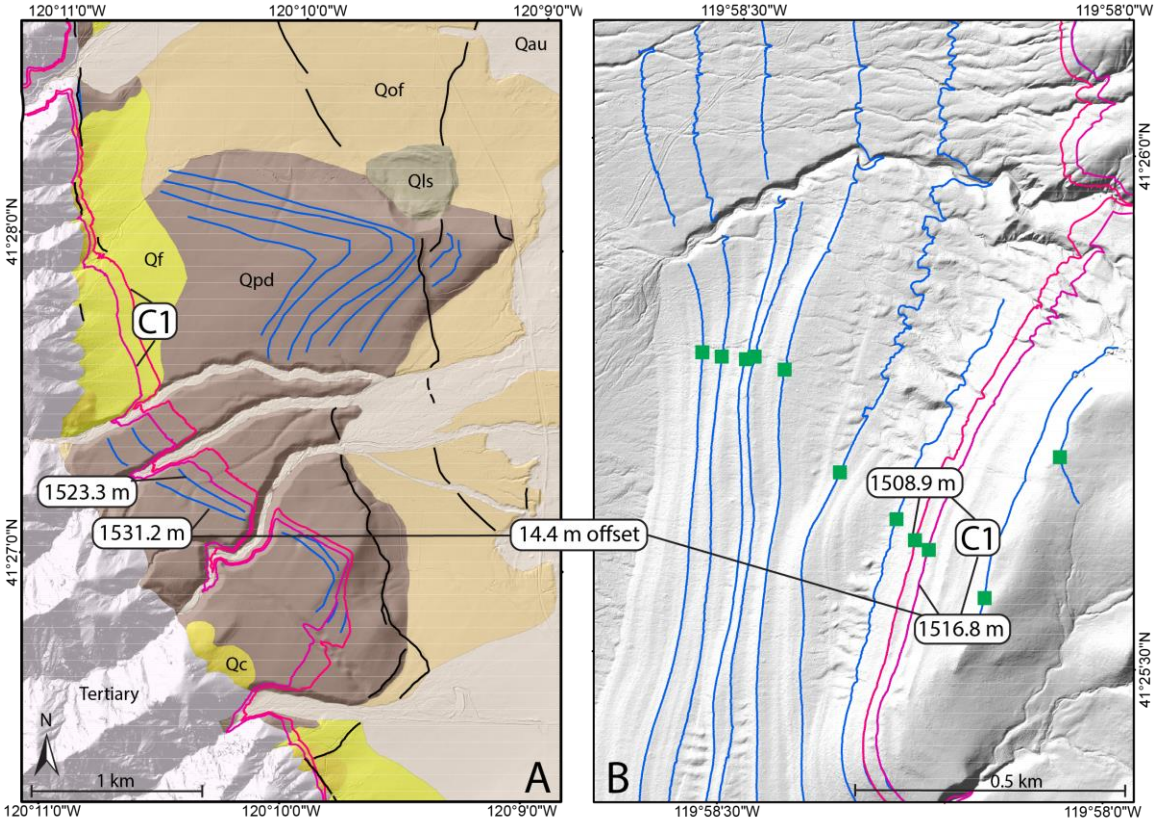

Figure 10. These figures correspond with the boxes labeled 10a and 10b in Figure 4. Black lines show the Surprise Valley fault scarps. Blue lines show the mapped paleoshoreline features. Colored contour lines have been added and they show the elevations of shorelines that have been dated using 14C AMS analysis. Specific shorelines used for vertical offset are labeled by their present day elevations. Using the known shoreline ages and elevations, I have correlated shoreline packages along the western side of the valley with the in situ shoreline packages along the eastern side.

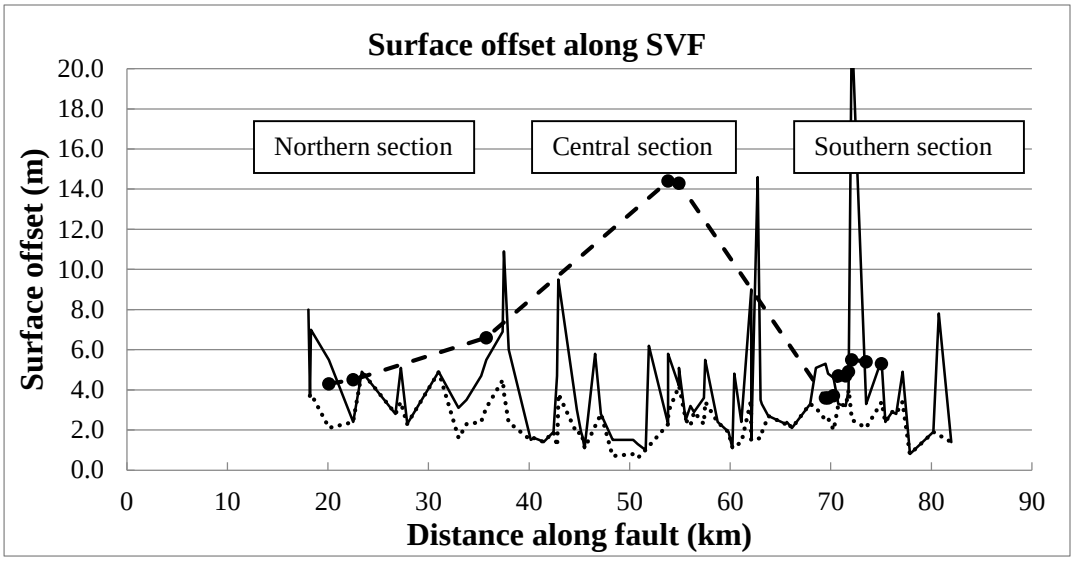

Figure 11**.** The dotted line represents the offset from the most recent interpreted event at 1.2 ka with offset between 1 and 5 m along the SVF, from Egger (2014). The solid line is the total offset across topographic profiles of SVF scarps, from Egger (2014). The dashed line is the measured offset using paleoshoreline sets across the valley.

Table 5. Paleoshoreline Offset Measurements

Lake Section	Vertical offset (m)	Shoreline set	Distance along fault N to S (km)	Slip at 60º (m)	Slip at 68º (m)	Slip at 35º (m)
Northern lake	4.3 ± 0.4	N1	20.1	5.0 ± 0.4	4.6 ± 0.5	7.5 ± 0.7
	4.5 ± 0.4	N1	20.1	5.2 ± 0.5	4.9 ± 0.4	7.8 ± 0.7
	6.6 ± 0.7	N1	35.7	7.6 ± 0.9	7.1 ± 0.9	12 ± 0.9
Central lake	14.4 ± 1	C1	54.5	16.6 ± 1.0	15.5 ± 1.0	25.1 ± 2.0
	14.3 ± 1	C1	54.7	16.5 ± 1.0	15.4 ± 1.0	25.0 ± 2.0
Southern lake	3.6 ± 0.2	S1	70.0	4.2 ± 0.2	3.9 ± 0.2	6.3 ± 0.3
	3.7 ± 0.2	S1	70.0	4.3 ± 0.2	4.0 ± 0.2	6.5 ± 0.3
	4.7 ± 0.3	S2	71.5	5.4 ± 0.3	5.1 ± 0.3	8.2 ± 0.5
	4.9 ± 0.3	S2	71.5	5.7 ± 0.3	5.3 ± 0.3	8.5 ± 0.5
	5.3 ± 0.5	S1	73.5	6.1 ± 0.6	5.7 ± 0.6	9.2 ± 0.9
	5.4 ± 0.5	S1	73.5	6.2 ± 0.6	5.8 ± 0.6	9.4 ± 0.9
	5.5 ± 0.5	S1	73.5	6.4 ± 0.5	5.9 ± 0.5	9.6 ± 0.9

Slip Rate Calculations

Using the measured offsets and the ages of paleoshorelines from this study and Ibarra et al. (2014), I calculated the average slip rate (Table 6). These slip rates are inferred based on inferred offset across all fault scarps including the SVF and intra-basin fault strands using paleoshorelines as an indirect marker of offset. I have calculated slip

rate using vertical offset measurements by assuming three different dips for the SVF of 60°, 68°, and 35°. Bold values in Table 6 represent the preferred slip rates since the most recent highstand, calculated using the youngest shorelines.

Table 6. Slip Rate Calculations

Lake section	Vertical offset (m)	Time period (ka)	Slip rate at 68º (mm/yr)	Slip rate at 60º (mm/yr)	Slip rate at 35º (mm/yr)	Vertical Slip rate (mm/yr)
Northern	4.3 ± 0.4	19.22 ± 0.23	0.24 ± 0.03	0.26 ± 0.03	0.39 ± 0.04	0.22 ± 0.03
	4.5 ± 0.4	19.22 ± 0.23	**0.25 ± 0.02**	0.27 ± 0.03	0.41 ± 0.04	0.23 ± 0.03
	6.6 ± 0.7	22.08 ± 0.26	0.32 ± 0.04	0.35 ± 0.04	0.52 ± 0.06	0.30 ± 0.03
Central	14.4 ± 1	14.53 ± 0.35	**1.07 ± 0.05**	1.14 ± 0.06	1.73 ± 0.07	1.00 ± 0.05
	14.3 ± 1	14.53 ± 0.35	1.06 ± 0.05	1.14 ± 0.05	1.72 ± 0.07	0.98 ± 0.04
Southern	4.7 ± 0.3	14.53 ± 0.35	0.35 ± 0.02	0.37 ± 0.04	0.56 ± 0.05	0.32 ± 0.03
	4.9 ± 0.3	14.53 ± 0.35	**0.36 ± 0.04**	0.39 ± 0.03	0.59 ± 0.05	0.34 ± 0.03
	5.3 ± 0.5	17.21 ± 0.23	0.33 ± 0.04	0.36 ± 0.03	0.54 ± 0.04	0.31 ± 0.03
	5.4 ± 0.5	17.21 ± 0.23	0.34 ± 0.03	0.36 ± 0.03	0.55 ± 0.06	0.31 ± 0.04
	5.5 ± 0.5	17.21 ± 0.23	0.34 ± 0.04	0.37 ± 0.04	0.56 ± 0.06	0.32 ± 0.03

The slip rate in the northern section was calculated at 0.3 ± 0.03 mm/yr over the last 19.22 ± 0.23 ka. Using another location for shoreline set N1 that had 6.6 m of slip, I calculated a slip rate of 0.3 ± 0.04 mm/yr over the last 22.08 ± 0.26 ka period. Those ages were chosen because they represent the youngest age of shorelines within the shoreline set that was used to measure offset. This slip rate is lower (about half) than the 0.6 ± 0.1 mm/yr indicated by Personius et al. (2009).

The main shoreline sequence in the central section had a slip rate calculated using shoreline set C1 at 1.0 ± 0.1 mm/yr over the last 14.53 ± 0.35 ka period. The 14.53 ka age was chosen as it represents the youngest shoreline age included in the shoreline set. This slip rate is nearly twice the rate reported by earlier studies or at any other locations in this study.

In the southern section, slip rate calculated using shoreline set S2, was between 0.4 ± 0.03 mm/yr over the last 14.53 ± 0.35 ka, and the slip rate calculated from shoreline set S1 ranged between 0.3 ± 0.03 mm/yr over the last 21.43 ± 0.26 ka. Those ages for slip rate calculations were chosen for shoreline sets S1 and S2 as they were the youngest shorelines within the shoreline sets. These are also lower than the previously published slip rates. Uncertainties on the slip rates are carried through from the uncertainties on the calibrated ages of the shorelines, and uncertainties on measuring offset using the DEM.

Geophysical Modeling

Locations of the profiles are given in Figures 12 and 13. Figures 14 and 15 show best fit models for Profiles A (Northern section) and B (Central section) respectively. Features of interest in both profiles A and B are the significant dips in the observed magnetic profile directly to the left of the SVF surface trace. This magnetic low was the most challenging to replicate with potential field modeling. These lows in the observed magnetic profile are interpreted as hydrothermal demagnetization of the rock units directly in contact with the surface trace of the SVF.

For both models (Figures 14 and 15) I have produced a reasonably good fit for the observed gravity profiles. For model A, (Figure 14) there is a large error between the observed and calculated magnetic profiles that begins at ~3 km. The sharp drop in the observed magnetic profile was ultimately ignored in the 2D potential field model, as I was only focused on modeling the SVF at shallow depths directly across the fault scarp and the magnetic drop was considered as too far away from the area of interest to have

any effect on the model. A potential inclusion in the model to fit the calculated magnetic profile to the observed would be to include a shallow, reversed basalt flow extending out into the basin from the western side as modeled in Egger et al. (2009).

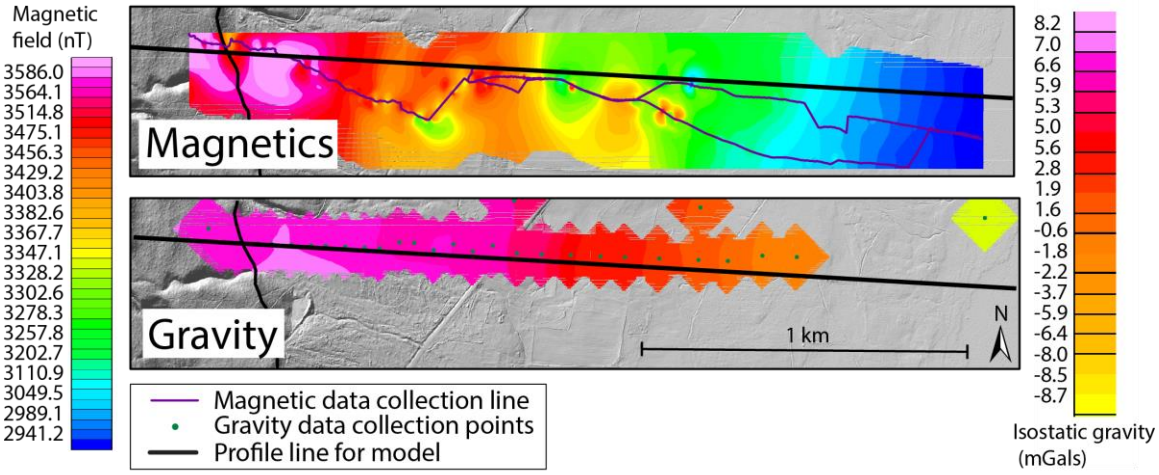

Figure 12. Location figure for Profile A, a 2D potential field model formed in this study. The top figure is the gridded magnetic data from a truck-towed magnetometer transect. The bottom figure is the gridded gravity data. The location of this figure is detailed in Figure 4 with the black box labeled '12'. Both magnetic and gravity data are limited by the extent of detailed data along a straight-line transect.

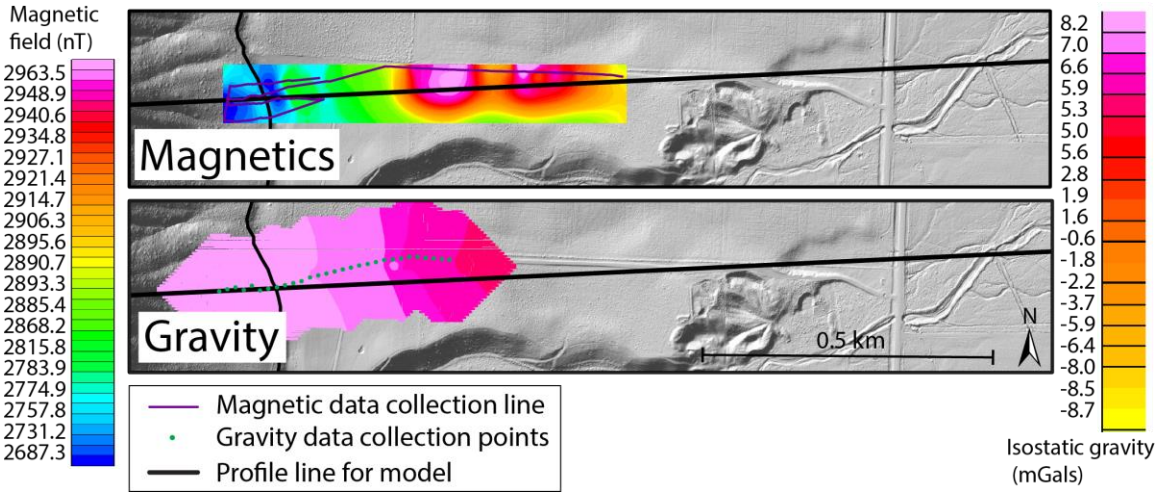

Figure 13. Location figure for Profile B, a 2D potential field model formed in this study. The top figure is the gridded magnetic data from a truck-towed magnetometer transect. The bottom figure is the gridded gravity data. The location of this figure is detailed in Figure 4 with the black box labeled '13'. Both magnetic and gravity data are limited by the extent of detailed data along a straight-line transect.

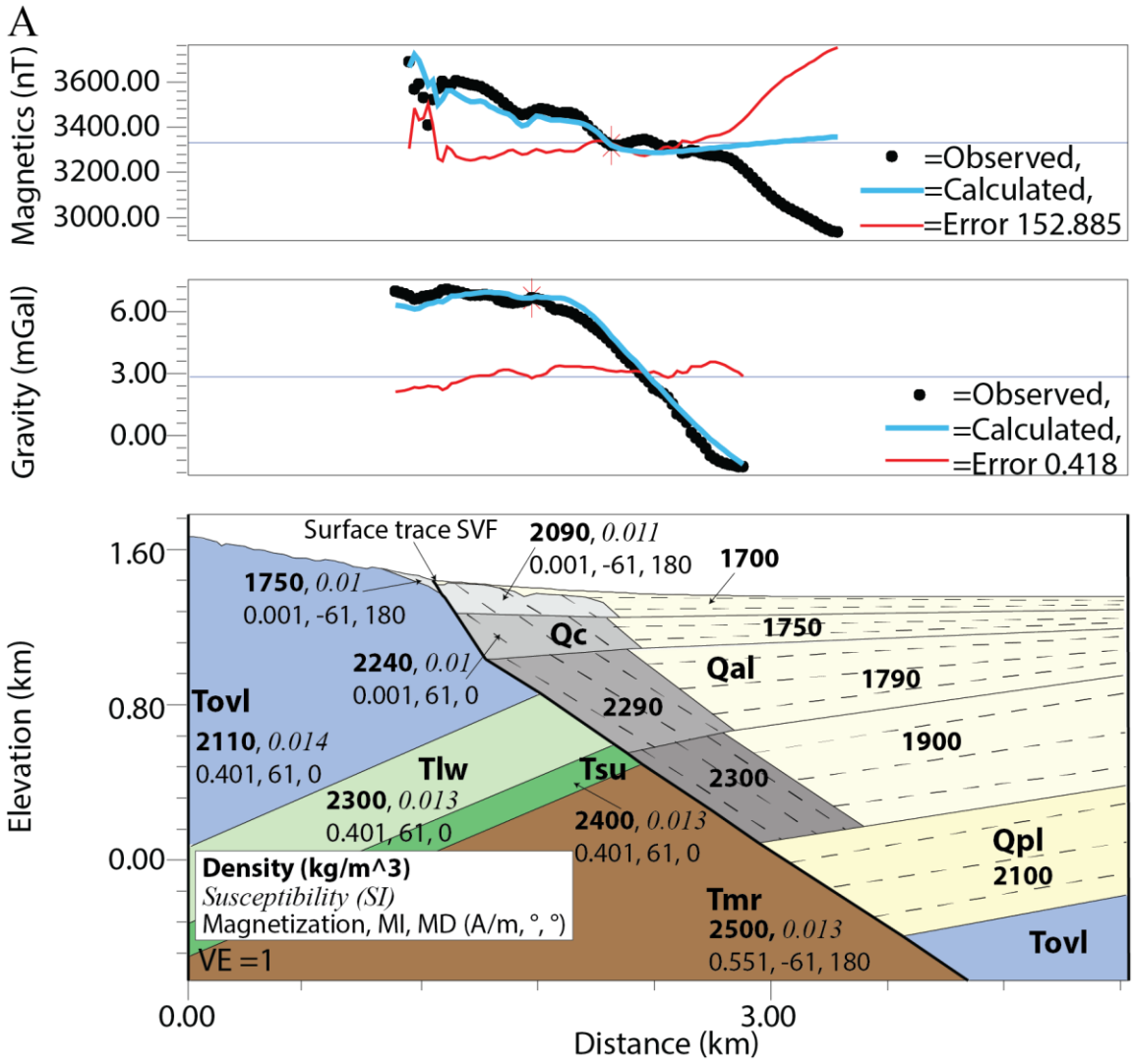

Figure 14. Potential field model A. Units labeled Qal, Qc, Qpl, Tmr, Tovl, Tlw, and Tsu correspond to geologic units detailed in Egger and Miller, 2011. Inferred faults are shown in bolded lines. Density Inclination and Declination labeled MI and MD respectively.

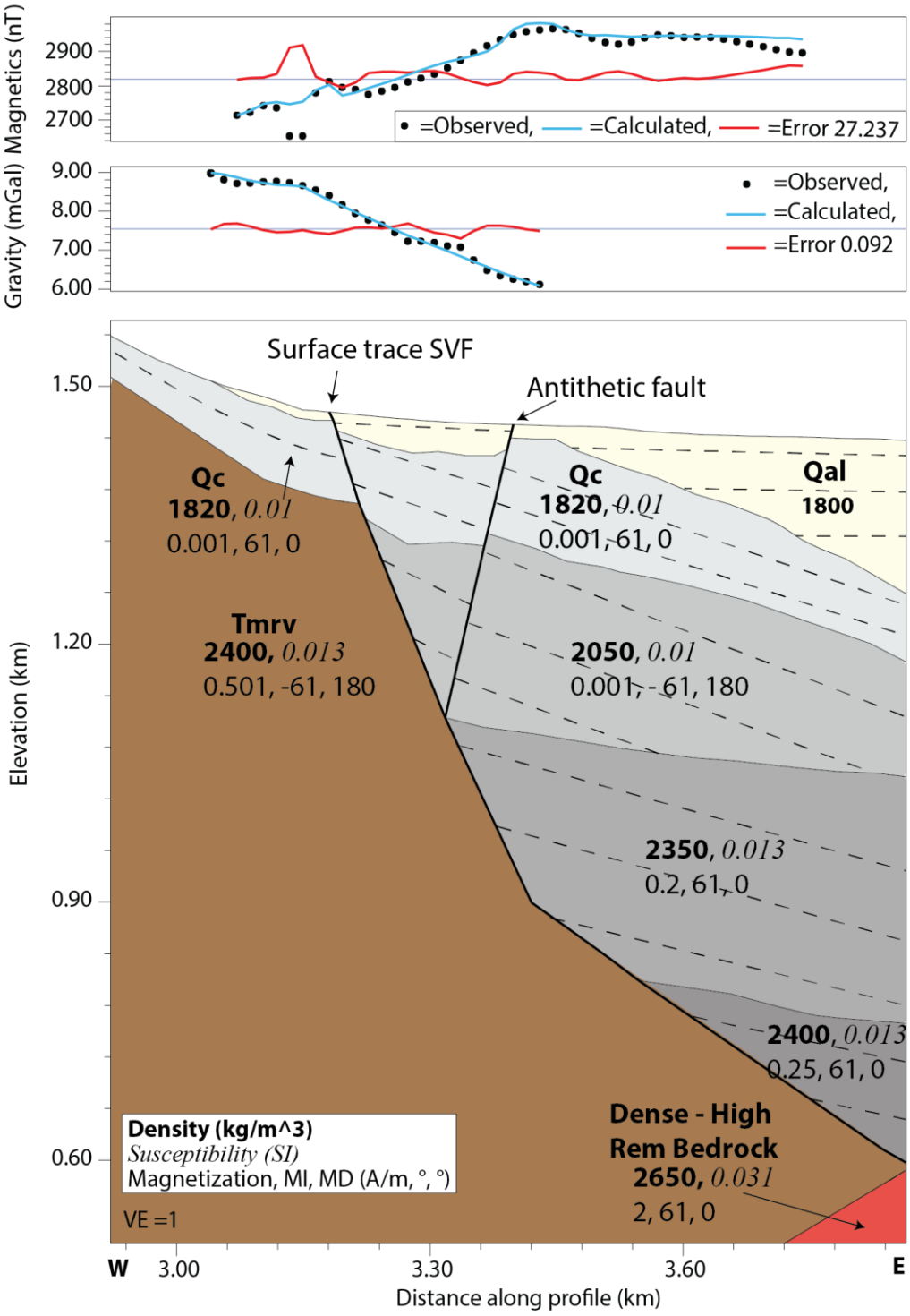

Figure 15. Potential field model B. Units labeled Qal, Qc, and Tmrv correspond to geologic units detailed in Egger and Miller, 2011. Inferred faults are shown in bolded lines. Magnetic inclination and declination labeled MI and MD respectively.

Approximately 1.8 km along the profile in the least dense Qc unit, I modeled a small notch to match a similar dip in the observed magnetic and gravity profiles that would be explained with the presence of a steeply-dipping basinward fault strand that links to the SVF at depth. It wasn't necessary to model a fault with a measurable amount of offset in that location to fit the observed profiles; however, a fault would explain the sharp change in elevation modeled in the notch of Qc. In model A (Figure 14), due to the nature of using blocks to model various rock units magnetic and density properties, the contacts between Qc and Qal is modeled as a sharp, distinct boundary. The modeled contact is meant to be more transitional from colluvial deposition to alluvial deposition. The places between 2 and 3.5 km where Qc and Qal overlap were modeled as such to illustrate the alternating nature of range front colluvium and basin alluvium deposits.

In model B (Figure 15), in order to fit the observed magnetic and gravity profiles, a steeply-dipping antithetic fault was inserted to offset the youngest Qc and Qal units. This antithetic fault does not have a surface expression.

From model A (Figure 14) using the Tertiary Lost Woods (Tlw) formation as a marker bed across the SVF, I measured 5.35 km of slip along a 35° dip fault of the Oligocene (23.03 - 33.9 Ma (Cohen et al., 2013)) Tlw formation (Egger and Miller, 2011). I measured vertical offset across the modeled Qc deposits in model B (Figure 15). Offset measured across the SVF was 18 m, while offset across the antithetic fault was 14 m (Figure 15). Slip was calculated from the vertical offset measurements using a 68° dip of the fault, for the SVF, 20 m of slip, and for the antithetic fault, 16 m of slip.

Using the geophysical models as a tool for calculating slip rate provides similar results. Model A (Figure 14) measures a slip of 5.35 km along a 35° fault of Oligocene units. Using the age of initiation of the fault of 12 Ma (Colgan et al., 2006), I calculated a long term slip rate at 35° for the northern segment of 0.45 mm/yr. For the vertical offset rate, the Tlw formation was offset vertically 3.07 km and using the same initiation age of 12 Ma, I calculated a vertical offset rate of 0.26 mm/yr, and a slip rate along a 68° fault at 0.28 mm/yr.

CHAPTER V

DISCUSSION

Figure 15 summarizes all of the results from this study and provides the basis for interpretation. Measured paleoshoreline offset, slip and slip rate are the greatest in the central section of the SVF; and all three die out towards the fault tips, as expected (Dawers et al., 1993; Figure 16). Slip is distributed asymmetrically, with the southern section showing more vertical offset of paleoshorelines than the northern section, and with the central section having its greatest offset closer to the southern extent of the fault than the northern portion (Figure 16).

This abrupt change in slip between the southern and central sections with the northern section could be attributed to the boundary between the northern and central section being the largest structural discontinuity along the SVF (Figure 17). The larger the structural discontinuity, the larger an earthquake rupture has to be in order to not be stopped by the discontinuity (Zhang et al., 1999). This boundary is an en echelon left-step as a strand of the SVF extends out into the basin 2.5 km away from the range front (Figure 17). This suggests the central and southern segments are acting independently from the northern segment and may be a barrier to earthquake rupture (Figure 17). Fault scarps along ~42 km of the ~90 km long fault are interpreted to represent the surface rupture of the most recent event; these range in offset from 1.0–4.0 m (Egger, 2014).

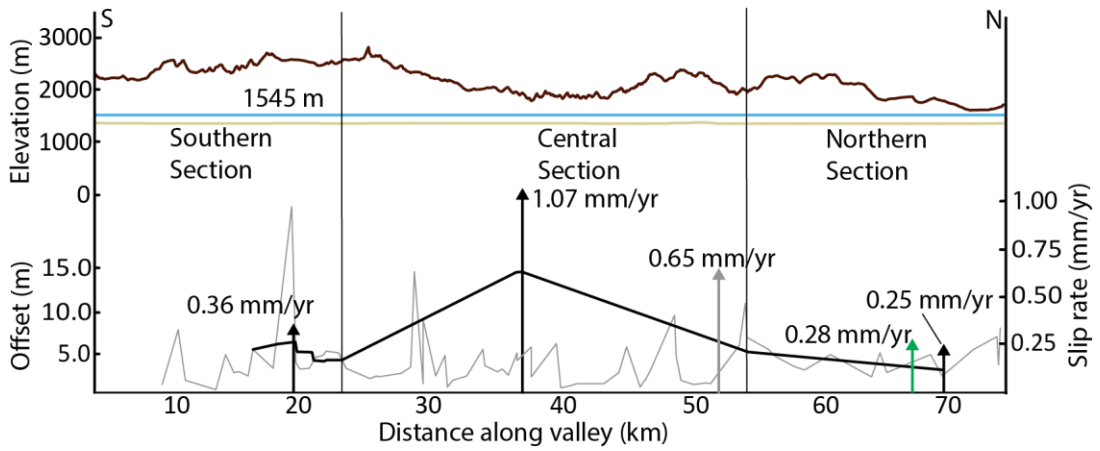

Figure 16**.** Slip rate distribution for SVF. N-S topographic profile along the Warner Range (brown), and the Surprise Valley playa (tan). Elevation of Lake Surprise highstand at 1545 m (blue). Total offset of topographic profiles of SVF scarps (grey) and measured offset using paleoshoreline sets across the valley (black). The labeled grey arrow represents the previously known slip rate along the entire fault (Personius et al., 2009). The black labeled arrows are the new variable slip rates calculated in this study for each section along the fault. The green arrow represents the calculated slip rate from the 2D potential field model for Profile A (Figure 14).

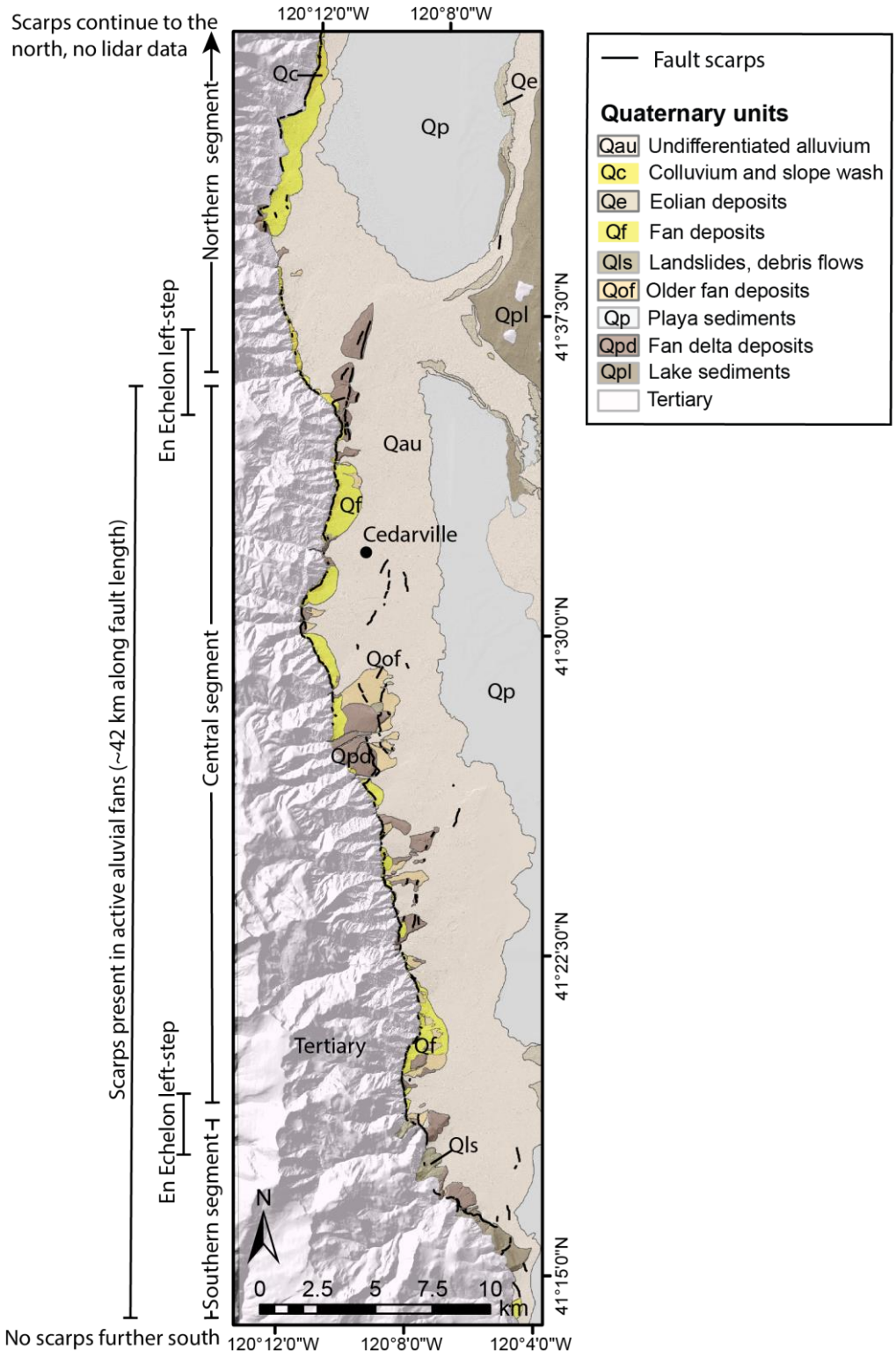

Figure 17. Geologic interpretation draped over a shaded relief map of Surprise Valley. Northern, Central, and Southern segments of the SVF are marked.

The total offset measured by paleoshorelines is greater than the offset along the scarps in the central segment, while within the northern and southern segments, measured paleoshoreline offset is similar to offset measured along the scarps. It is possible that these discrepancies are related to the nature of fault scarps and how they degrade over time. To use fault scarps as an accurate proxy for surface offset, the only erosional force acting on the scarp must be gravity (McCalpin, 2009). Scarps of a given age that cut through different materials will tend to form scarps of different height (McCalpin, 2009). Scarps in the central section that predominantly cut through active alluvial fan deposits, measure less offset than scarps in the central section that cut through Pleistocene lake deltas (Egger, 2014). Scarps in finer-grained materials degrade more quickly and have a lower maximum slope angle for a given height than scarps in coarser-grained materials (Dodge, 1982). Along the central SVF, scarps in active alluvial fans possibly could have not formed fault scarps as high as scarps in other sediments. Using paleoshorelines across the basin as a marker for total offset is not without its own assumptions. Even though this study treats paleoshorelines as horizontal markers, a single paleoshoreline has been shown to vary up to 2 m in elevation related to the inner edge relationship to the water surface during formation (Hopkins and Dawers, 2016).

A second explanation for the difference in total offset of scarps and paleoshorelines in the central segment is the presence of subsurface structures in the basin that could be accommodating the offset (Figure 15). Magnetic and gravity transects across the valley have suggested multiple intra-basin faults that do not have surface expressions (Egger et al., 2009; Athens et al., 2015). These represent strands that steepen

towards the surface of the main, active SVF that was imaged at a shallow angle at depth (Lerch et al., 2009; Egger et al., 2009).

It is possible that the shorelines that I have used to measure offset and calculate slip rate with in this study have not been correlated properly. Because we were unable to acquire radiocarbon ages for shorelines along the western side of the valley, I could not make absolute correlations. This is most apparent with the central section offset. Without ages of shorelines along the western side or other shoreline outcrops within the central segment to correlate with, the anomalously high offset of 14.4 m presents a potential source of error for this method. However, the elevation differences and geomorphological expression were similar, and they were consistently offset in the same direction, implying uplift of the mountain range and down dropping of the valley.

SVF Slip Rate

Several assumptions have been made in order to utilize paleoshorelines and the magnetic/gravity models for slip rate calculations. First, paleoshorelines that are older than 18 ± 2 ka (the age of earthquake event PX) carry the potential of being offset during the PX event, relative to shorelines that formed after the lake highstand. This potential offset would change the relative spacing between the older shorelines with the shorelines that will not have formed until after event PX. Second, the slip rate calculated with Profile A (Figure 14) draws upon assumptions of the age of initiation for the SVF, along with assumptions regarding the thickness of the units mapped on the surface, and then modeled in the subsurface.

Through the paleoshoreline method, I have calculated the varying vertical slip-rate along strike of the SVF of 0.25 ± 0.02 mm/yr in the north, 1.07 ± 0.05 mm/yr in the center, and 0.36 ± 0.04 mm/yr in the south (Figure 16). These slip rates represent how active SVF has been since the Last Glacial Maximum. In comparison, Personius et al (2009) calculated vertical slip rates between earthquakes, and the slip rate between events P4 and P2 was calculated at 1.0 ± 0.7 mm/yr, the same value as my calculations for the central segment but with much great uncertainty. This suggests that paleoshorelines can provide not only an accurate but more precise measuring tool for slip and slip rate calculations.

In the northern lake basin, which is a half-graben (Figure 18), the lower slip rate could be attributed to the presence of multiple faulting structures that are accommodating the slip, such as the faults in the Larkspur hills to the east (Strickley and Egger, 2014) (Figure 18). The central and southern basins of Surprise Valley form a full graben, bounded by the SVF to the west, and the Hays Canyon fault to the east. Across the basin from the northern-central segment boundary, the Hays Canyon Fault transitions into the Larkspur Hills accommodation zone and the northern basin forms a half-graben. Normal faulting systems that share this relationship with half-graben segmentation and sub-parallel migration basinwards into the original hanging walls, have been demonstrated in many other places, including large systems such as the East African rift (Faulds and Varga, 1998) and mainland Greece (Goldsworthy and Jackson, 2001) as well as within other portions of the Basin and Range, including the Black Mountains zone (Faulds et al., 1990). Kinematic transferring of slip can be occurring from the northern SVF segment to

the Larkspur Hills normal and strike-slip faults. There are no scarps along the Larkspur Hills faults, so they haven't been active during the Holocene (unlike the SVF). Despite this, they are still candidates for the kinematic transferring of slip because they are faults working on longer timescales (10^6 yrs) than the recent activity along the SVF (10^4 yrs) (Strickley and Egger, 2014) **(**Figure 18).

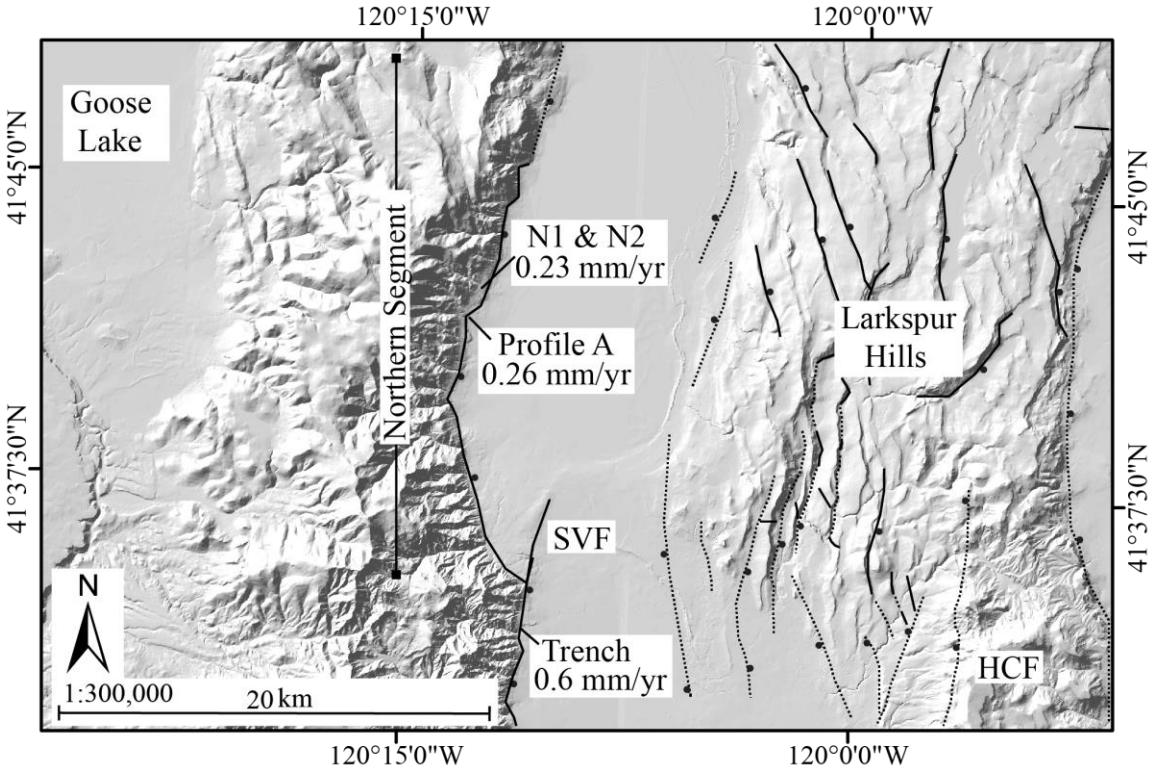

Figure 18. Map of the northern segment showing the numerous faults within the Larkspur Hills and the disparity between the trench vertical slip rate (Personius et al., 2009) and the northern segments vertical slip rate calculations from this study. Black and dotted lines are mapped and inferred fault locations from Egger and Miller, 2011. Slip rates stated in the figure are vertical slip rates for comparison with the Personius et al., 2009 trench study. I propose that the Larkspur Hills accommodation zone for the Hays Canyon Fault (labeled HCF in the figure) is an accessible location for the kinematic transferring of slip from the SVF in the northern segment.

Through modeling, I was able to quantify offset along the SVF to a greater depth than through trenching and paleoshoreline offsets alone. From Model B, along the SVF I modeled 18 m of offset, which was 7 m greater than the offset able to be measured from a

trench across the fault at the same location (Personius et al., 2009). In addition, my modeled antithetic fault in Model B modeled 14 m of offset, which was not being captured through fault scarps since the fault does not leave a surface trace. The amount of offset along the antithetic fault suggests that it has been accommodating slip along the SVF for more than 25 ky, but its lack of surface expression suggests that it wasn't used in accommodating slip during the most recent major earthquake along the SVF 1.2 ± 0.1 ka.

We can expand upon the slip rates calculated using paleoshorelines by including a long-term, geologic slip rate of the SVF since its initiation in the late Miocene (Colgan et al., 2008; Egger and Miller, 2011). The calculated vertical slip rate for the northern section is 0.26 mm/yr over 12 My. This slip rate is comparable with the northern segment calculated at 35° with paleoshorelines of 0.23 ± 0.03 mm/yr. The similarity of the short-term and long-term slip rates for the northern segment suggest that the kinematics for faulting have remained relatively constant since fault initiation. The effect of pluvial Lake Surprise had upon the northern segment of the SVF appears to be minimal when compared with the long term average of slip rate in the northern section. We do see a slight decrease in slip rate during periods of lake recession, which could be attributed to Lake Surprise. This idea is supported through slip rate modeling along the Wasatch fault in central Utah were the segments of the fault furthest to the north and south of Lake Bonneville during the Pleistocene, experienced minimal changes in slip rate when compared to the fault segments towards the center of the lake (Karow and Hampel, 2010).

The topographic profile along the length of the Warner Range (Figure 16) shows low elevation section toward the center of the profile, despite the higher slip rate and offset of paleoshorelines. With my calculated faster slip rate in the central segment, we would expect more uplift in the range in this segment. With this increased in uplift, we would also expect greater relief and older rocks exposed. This is the portion of the range where the oldest rocks—Eocene in age—are exposed (Egger and Miller, 2010), however, the relief along the center segment is lower than the relief to both the north and south. To explain this, I offer a few possibilities: (1) the slip rate in the central segment only recently became faster than the southern segment, which has a much greater relief in the range; (2) my calculated slip rate of 1.07 ± 0.05 mm/yr in the central segment is incorrect; or (3) erosion is happening faster in the central part of the range, or (3) my calculated slip rate of 1.1 mm/yr in the central segment is incorrect. Because slip is generally greater at the center of normal faults, it is unlikely that (1) explains the topographic low in the range (Zhang et al., 1999; Machette et al., 1991; Peacock and Sanderson, 1991; Dawers et al., 1993). It is unlikely that (2) is correct as well, given the confidence and consistency in using paleoshorelines as an offset and slip rate tool. This low relief could be attributed to a change in lithology from the northern and southern extents of the range to the center of the range. The northern and southern sections consist primarily of Miocene and Oligocene basaltic lava flows while the central section is predominately pyroclastic flows and less resistant tuff deposits, making it more susceptible to erosion (Egger and Miller, 2011).

During the period of pluvial lake recession, we see an overall increase in slip rate in the center segment, and a decrease of slip rate in the northern and southern segments of the SVF from the long-term average. The slip rate distribution across the southern, central and northern segments can lead to two main interpretations. One possible interpretation is that this variability in slip rate could be attributed to standard normal fault mechanics, in that the highest slip and slip rate occurs in the center of the fault and that the slip and slip rate dies out towards the fault tips (Zhang et al., 1999; Machette et al., 1991). Due to the slip rates in the northern, central and southern segments averaging to 0.6 mm/yr, the variability in slip rate along strike of the SVF could be more simply attributed to the way normal faults demonstrate variability of slip rate along strike (Peacock and Sanderson, 1991; Dawers et al., 1993). This relationship between the shoreline slip rate calculations and the previously assumed long-term slip rates for this fault confirms the values that I have calculated in this study for slip rate and as well as the slip rates that have been previously assumed for the entire length of the SVF.

The second interpretation is in the agreement with the model results for Lake Bonneville and Lahontan slip rate variations (Karow and Hampel, 2010). That is, during the recession of Lake Surprise, there was an increase in slip rate in the fault closest to the center of the former lake, and a decrease in slip rate along the fault near its northern and southern tips, at the edges of the pluvial lake. In the southern lake section, slip rates calculated on older paleoshoreline sets (~21 ka) are slower than slip rates calculated on the paleoshoreline sets that are ~14.5 ka. This change in slip rate between periods of lake impoundment and lake recession, while not definitive, provides a good basis for drawing

the connection of how Lake Surprise has impacted slip along the SVF and is supported through changes in slip rate evidence from trenching (Personius et al., 2009), and from paleoshoreline offsets and ages.

CHAPTER VI

CONCLUSION

Offset along the SVF has been shown to vary along strike using paleoshorelines as a horizontal marker. This method has allowed us to efficiently capture a sense of how offset varies along strike when used in conjunction with trench work and topographic scarp profile measurements. When compared with variable slip rate models along strike of nearby fault systems (Karow and Hampel, 2010) the recession of pluvial Lake Surprise may have had an appreciable influence on the slip rate along the SVF. The impoundment and recession of Lake Surprise has appeared to affect the recurrence of earthquakes (Figure 11) and slip rate through time as well (Figure 16). Like other nearby basins, the cycle of filling and receding pluvial lakes has profound effects on earthquake recurrence (Weldon, 2009) and slip rate (Karow and Hampel, 2010). The variable slip rate and clustering of earthquakes during the time of rapid lake depletion suggests that the Pleistocene lake could have played a role temporally in the evolution of SVF's history (Figure 16).

REFERENCES

Adams, K. D., & Wesnousky, S. G. 1998. Shoreline processes and the age of the Lake Lahontan highstand in the Jessup embayment, Nevada. *Geological Society of America Bulletin*, 110(10), 1318-1332.

Anderson, E. M. 1951. The Dynamics of Faulting, Etc.(Revised.). Edinburgh, London.

Badger, T. C., and Watters, R. J., 2004, Gigantic seismogenic landslides of Summer Lake basin, south-central Oregon: *Geological Society of America Bulletin*, v. 116, no. 5-6, p. 687-697.

Bell, L. M., and Nur, A., 1978, Strength Changes Due to Reservoir-Induced Pore Pressure and Stresses and Application to Lake Oroville: *Journal of Geophysical Research*, v. 83, no. B9.

Benoit, D., Moore, J. N., Goranson, C., & Blackwell, D. D. 2005. Core hole drilling and testing at the Lake City, California geothermal field. *Geothermal Resources Council Transactions*, 29, 203-208.

Blakely, R.J., 1995. Potential theory in gravity and magnetic applications. Cambridge University Press, New York. 441 pp

Briggs, I. C. 1974. Machine contouring using minimum curvature. *Geophysics*, 39(1), 39-48.

Bryant, W.A., 1990. Surprise Valley and related faults, Lassen and Modoc counties, Fault Evaluation Report, Sacramento, 17 p.

Carter, D. T., Ely, L. L., O'Connor, J. E., & Fenton, C. R. 2006. Late Pleistocene outburst flooding from pluvial lake Alvord into the Owyhee River, Oregon. *Geomorphology*, 75(3), 346-367.

Caskey, S. J., & Ramelli, A. R. 2004. Tectonic displacement and far-field isostatic flexure of pluvial lake shorelines, Dixie Valley, Nevada. *Journal of Geodynamics*, 38(2), 131-145.

Cohen, K.M., Finney, S.C., Gibbard, P.L. & Fan, J.-X. 2013; updated The ICS International Chronostratigraphic Chart. Episodes 36: 199-204.

Colgan, J. P., Dumitru, T. A., McWilliams, M., and Miller, E. L., 2006, Timing of Cenozoic volcanism and Basin and Range extension in northwestern Nevada: New constraints from the northern Pine Forest Range: *Geological Society of America Bulletin*, v. 118, no. 1-2, p. 126-139.

Colgan, J. P., Shuster, D. L., & Reiners, P. W. 2008. Two-phase Neogene extension in the northwestern Basin and Range recorded in a single thermochronology sample. *Geology*, *36*(8), 631-634.

Crittenden, M. D. 1963. Effective viscosity of the earth derived from isostatic loading of Pleistocene Lake Bonneville. *Journal of Geophysical Research*, 68(19), 5517-5530.

Crozier, M.J., 1992, Determination of paleoseismicity from landslides, *in* Bell, D.H., ed., Proceedings, Landslides (Glissements de terrain), Volume 2, 6th International Symposium, Christchurch, New Zealand: Rotterdam, A.A. *Balkema*, p. 1173–1180.

Dawers, N. H., Anders, M. H., & Scholz, C. H. 1993. Growth of normal faults: Displacement-length scaling. *Geology*, 21(12), 1107-1110.

Dodge, R. L., 1982, Seismic and Geomorphic History of the Black Rock Fault Zone, Northwest Nevada. (Doctoral thesis, Colorado School of Mines)

Egger, A. E., 2014, Paleoearthquake Magnitudes Derived from Lidar Based Mapping of Fault Scarps in the Northwestern Basin and Range: GSA Annual Meeting in Vancouver, British Columbia.

Egger, A. E., and Ibarra, D. E., 2012, Paleoseismology from Paleoshorelines: Combining lidar data and geochronology to resolve displacement of Pleistocene pluvial shorelines along normal faults in the northwestern Basin and Range. Abstract PP11A-2003 presented at 2012 Fall Meeting, AGU, San Francisco, Calif., 3-7 Dec.

Egger, A. E., and Miller, E. L., 2011, Evolution of the northwestern margin of the Basin and Range: The geology and extensional history of the Warner Range and environs, northeastern California: *Geosphere*, v. 7, no. 3, p. 756-773.

Egger, A. E., Glen, J. M., & Ponce, D. A. 2009. The northwestern margin of the Basin and Range province: Part 2: Structural setting of a developing basin from seismic and potential field data. *Tectonophysics*, 488(1), 150-161

Faulds, J. E., Geissman, J. W., & Mawer, C. K. 1990. Structural development of a major extensional accommodation zone in the Basin and Range Province, northwestern Arizona and southern Nevada; Implications for kinematic models of continental extension. *Geological Society of America Memoirs*, 176, 37-76.

Faulds, J. E., & Varga, R. J. 1998. The role of accommodation zones and transfer zones in the regional segmentation of extended terranes. *SPECIAL PAPERS-GEOLOGICAL SOCIETY OF AMERICA*, 1-46.

Felton, A., Jewell, P.W., Chan, M., and Currey, D., 2006, Controls of tufa development in Pleistocene Lake Bonneville, Utah: *The Journal of Geology*, v. 114, p. 377–389, doi: 10 .1086 /501218.

Gilbert, G. K. 1890. Lake Bonneville (Vol. 1). US Government Printing Office.

Glen, J.M.G., Egger, A.E., and Ponce, D.A., 2008, Structures controlling geothermal circulation identified through gravity and magnetic transects, Surprise Valley, California, northwestern Great Basin: Geothermal Resources Council Transactions, v. 32, p. 279-283.

Goldsworthy, M., & Jackson, J. 2001. Migration of activity within normal fault systems: examples from the Quaternary of mainland Greece. *Journal of Structural Geology*, 23(2), 489-506.

Gupta, H. K. 2002. A review of recent studies of triggered earthquakes by artificial water reservoirs with special emphasis on earthquakes in Koyna, India. *Earth-Science Reviews*, 58(3), 279-310.

Hampel, A., & Hetzel, R. 2006. Response of normal faults to glacial-interglacial fluctuations of ice and water masses on Earth's surface. *Journal of Geophysical Research: Solid Earth*, 111(B6).

Hampel, A., Hetzel, R., & Maniatis, G. 2010. Response of faults to climate-driven changes in ice and water volumes on Earth's surface. Philosophical Transactions of the Royal Society of London A: Mathematical, Physical and Engineering Sciences, 368(1919), 2501-2517.

Hedel, C. W., 1980, Late Quaternary faulting in western Surprise Valley, Modoc County, California [M.S. Master's]: San Jose State University, 142 p.

Henry, C. D., & Perkins, M. E. 2001. Sierra Nevada–Basin and Range transition near Reno, Nevada: two-stage development at 12 and 3 Ma. *Geology*, 29(8), 719-722.

Hopkins, M. C., & Dawers, N. H. 2016. Vertical deformation of lacustrine shorelines along breached relay ramps, Catlow Valley fault, southeastern Oregon, USA. *Tectonophysics*, 674, 89-100.

Ibarra, D. E., Egger, A. E., Weaver, K. L., Harris, C. R., and Maher, K., 2014, Rise and fall of late Pleistocene pluvial lakes in response to reduced evaporation and

precipitation: Evidence from Lake Surprise, California: *Geological Society of America Bulletin.*

Karow, T., & Hampel, A. 2010. Slip rate variations on faults in the Basin-and-Range Province caused by regression of Late Pleistocene Lake Bonneville and Lake Lahontan. *International Journal of Earth Sciences*,99(8), 1941-1953.

Karow, T. 2009. Three-dimensional finite-element modeling of slip rate variations on faults caused by glacial–interglacial changes in ice and water volumes: parameter study and application to nature (Doctoral dissertation, Doctoral thesis, Ruhr University).

Kell-Hills, A., Thompson, M., Dhar, M., Louie, J., Egger, A., van Buer, N., & Pullammanappallil, S. 2008, December. A complementary study of the Surprise Valley fault using a high-resolution shallow seismic reflection profile. In AGU Fall Meeting Abstracts (Vol. 1, p. 1968).

Kreemer, C., Hammond, W. C., Blewitt, G., Holland, A. A., and Bennet, R. A., 2012, A Geodetic Strain Rate Model for the Paci c-North American Plate Boundary, Western United States: Nevada Bureau of Mines and Geology.

Lerch, D. W., Klemperer, S. L., Egger, A. E., Colgan, J. P., & Miller, E. L. 2009. The northwestern margin of the Basin-and-Range Province, part 1: Reflection profiling of the moderate-angle (~ 30) Surprise Valley Fault. *Tectonophysics*, 488(1), 143-149.

Lerch, D.W., Klemperer, S.L., Glen, J.M.G., Ponce, D.A., Miller, E.L., and Colgan, J.P., 2006, Crustal structure of the northwestern Basin and Range Province and its transition to unextended volcanic plateaus: *Geochemistry, Geophysics, and Geosystems*, v. 8, no. 7, 21 p.

Lerch, D. W., Miller, E., McWilliams, M., and Colgan, J., 2008, Tectonic and magmatic evolution of the northwestern Basin and Range and its transition to unextended volcanic plateaus: Black Rock Range, Nevada: *Geological Society of America Bulletin*, v. 120, no. 3-4, p. 300-311.

Licciardi, J. M. 2001. Chronology of latest Pleistocene lake-level fluctuations in the pluvial Lake Chewaucan basin, Oregon, USA. *Journal of Quaternary Science*, 16(6), 545-553.

Machette, M. N., Personius, S. F., Nelson, A. R., Schwartz, D. P., & Lund, W. R. 1991. The Wasatch fault zone, Utah—segmentation and history of Holocene earthquakes. *Journal of Structural Geology*, 13(2), 137-149.

McCalpin, J. P. (Ed.). 2009. *Paleoseismology* (Vol. 95). Academic press.

Miller, E.L., Colgan, J.P., Surpless, B.E., Riedel-Bash, S., Strickland, A., Egger, A.E., Benoit, D., 2005. Drill core data from the Warner Range and Surprise Valley. Abstracts with Programs — Geological Society of America 37 (7), 203–204.

Nakiboglu, S. M., & Lambeck, K. 1983. A reevaluation of the isostatic rebound of Lake Bonneville. *Journal of Geophysical Research: Solid Earth*, 88(B12), 10439-10447.

Negrini, R.M., 2002, Pluvial lake sizes in the northwestern Great Basin throughout the Quaternary Period, in Hershel, R., ed., Great Basin Aquatic Systems History: Washington, D.C., Smithsonian Institute Press, p. 11–52.

Negrini, R. M., & Davis, J. O. 1992. Dating late Pleistocene pluvial events and tephras by correlating paleomagnetic secular variation records from the western Great Basin. *Quaternary Research*, *38*(1), 46-59.

Oldow, J. S., & Singleton, E. S. 2008. Application of Terrestrial Laser Scanning in determining the pattern of late Pleistocene and Holocene fault displacement from the offset of pluvial lake shorelines in the Alvord extensional basin, northern Great Basin, USA. *Geosphere*, 4(3), 536-563.

Oviatt, C. G., Currey, D. R., & Sack, D. 1992. Radiocarbon chronology of Lake Bonneville, eastern Great Basin, USA. *Palaeogeography, Palaeoclimatology, Palaeoecology*, 99(3-4), 225-241.

Peacock, D. C. P., & Sanderson, D. J. 1991. Displacements, segment linkage and relay ramps in normal fault zones. *Journal of Structural Geology*, 13(6), 721-733.

Personius, S. F., Crone, A. J., Machette, M. N., Mahan, S. A., Kyung, J. B., Cisneros, H., & Lidke, D. J. 2007. Late Quaternary paleoseismology of the southern Steens fault zone, northern Nevada. *Bulletin of the Seismological Society of America*, 97(5), 1662-1678.

Personius, S. F., Crone, A. J., Machette, M. N., Mahan, S. A., and Lidke, D. J., 2009, Moderate rates of late Quaternary slip along the northwestern margin of the Basin and Range Province, Surprise Valley fault, northeastern California: *Journal of Geophysical Research*, v. 114, no. B09405, p. 17.

Personius, S.F., compiler, 2002, Fault number 831a, Winter Rim fault system, Slide Mountain section, in Quaternary fault and fold database of the United States: U.S. Geological Survey website, http://earthquakes.usgs.gov/hazards/qfaults, accessed 03/01/2016 09:08 PM.

Pezzopane, S. K., & Weldon, R. J. 1993. Tectonic role of active faulting in central Oregon. *Tectonics*, 12(5), 1140-1169.

Pezzopane, S.K., 1993, Active faults and earthquake ground motions in Oregon [Ph.D. thesis]: Eugene, University of Oregon, 208 p.

Ponce, D.A., Glen, J.M.G., Egger, A.E., Bouligand, C., 2009. Geophysical studies in the vicinity of Warner Mountains and Surprise Valley, Northeast California, Northwest Nevada, and Southern Oregon. U.S. Geological Survey Open-File Report.

Reheis, M. C., Adams, K. D., Oviatt, C. G., & Bacon, S. N. 2014. Pluvial lakes in the Great Basin of the western United States—a view from the outcrop. *Quaternary Science Reviews*, 97, 33-57.

Reheis, M., 1999, Highest Pluvial-Lake Shorelines and Pleistocene Climate of the Western Great Basin: Quaternary research, v. 52, no. 2, p. 196-205.

Reimer, P.J., and 29 others, 2013, IntCal13 and Marine13 radiocarbon age calibration curves 0–50,000 years cal B.P.: *Radiocarbon*, v. 55, p. 1869–1887, doi: 10 .2458/azu_js_rc .55 .16947.

Scarberry, K. C., Meigs, A. J., & Grunder, A. L. 2010. Faulting in a propagating continental rift: Insight from the late Miocene structural development of the Abert Rim fault, southern Oregon, USA. *Tectonophysics*, 488(1), 71-86.

Strickley, D., & Egger, A. 2014. Controls on Fault Geometry During Early Stages of Extension in the Larkspur Hills, Northwest Basin and Range.

Stuiver, M., and Reimer, J. 1993. Extended 14C data base and revised CALIB 3.014 C age calibration program. *Radiocarbon,* v. 35, 215-230.

Stuiver, M., and Reimer, P.J., 2005, Extended 14C database and revised Calib 5.0 14C age calibration program: *Radiocarbon*, v. 35, p. 215–230.

Swain, C. J. 1976. A FORTRAN IV program for interpolating irregularly spaced data using the difference equations for minimum curvature. *Computers & Geosciences*, 1(4), 231-240.

Weldon, R. J. 2009, October. An earthquake cluster followed the drying of Pleistocene Lake Chewaucan, Central Oregon basin and range. In 2009 Portland GSA Annual Meeting.

Weldon, R. J., Lippoldt, R. C., Scharer, K., Streig, A. R., Langridge, R. M., Madugo, C. M., Biasi, G. P., Dawson, T. E. 2013. A comparison of slip rate, recurrence interval, and slip per event on several well-characterized faults. 2013 AGU Fall Meeting.

Xiao, F. 2012. Did the Zipingpu Dam trigger China's 2008 earthquake? The scientific case. Probe International.

Zhang, P., Mao, F., & Slemmons, D. B. 1999. Rupture terminations and size of segment boundaries from historical earthquake ruptures in the Basin and Range Province. *Tectonophysics*, 308(1), 37-52.

Appendix B

Table B1. Shoreline Set Data Expanded

Shoreline set	Elevation (m)	Tufa sample name	Radiocarbon age (ka)
Northern Lake Section			
-	1429	SV15AE07	-
-	1430.6	SVDI11-T4	20.84 ± 0.21
-	1433.1	SVDI12-T15	19.47 ± 0.23
N1	1437.7	SV15AE06	22.08 ± 0.26
-	1443	SV15AE05	21.43 ± 0.26
N1	1453.5	SVDI11-T2	19.22 ± 0.23
-	1462	SV15AE01	18.8 ± 0.14
-	1470	SV15AE02	18.07 ± 0.18
-	1478.4	SVDI11-T14	12.70 ± 0.06
-	1491	SV15AE03	13.95 ± 0.16
-	1494	SV15AE04	-
-	1542.3	SVDI12-T17	-
-	1555.7	SVDI11-T18	16.00 ± 0.18
-	1564.2	SVDI12-T18	25.31 ± 0.30
-	1566.8	SVDI12T19	-
Center Lake Section			
-	1419.5	SVDI12-T1	21.22 ± 0.25
-	1427.8	SVDI12-T3	-
-	1439.0	SVDI12-T4	-
-	1443.0	SV15AE05	21.43 ± 0.26
-	1444.3	SVDI12-T5	10.69 ± 0.11
-	1458.5	SV15BM04	19.56 ± 0.22
-	1468.6	SV15BM05	-
-	1472.5	SVDI12-T7	-
-	1479.2	SV15BM06	-
-	1495.0	SV15BM07	-
C1	1508.9	SVDI12-T9	14.53 ± 0.35
C1	1516.8	SVDI12-T10	14.94 ± 0.24
-	1545.0	SV15AE12	15.98 ± 0.19
-	1554.9	SVDI12-T11	-
-	1576.9	SVDI12-T12	8.58 ± 0.07
Southern Lake Section			
-	1384	SV15AE08	-
S1	1427.8	SVDI12-T3	-
-	1437.2	SVDI12-T13	23.13 ± 0.30
S1	1437.7	SV15AE06	22.08 ± 0.26
S1	1440.2	SV15BM03	17.21 ± .023
-	1441	SV15BM08	21.46 ± 0.27
-	1445	SV15AE09	-
-	1456	SV15BM09	19.82 ± 0.21
-	1483	SV15AE10	-
-	1497	SV15AE11	-
S2	1508.9	SVDI12-T9	14.53 ± 0.35
S2	1516.8	SVDI12-T10	14.94 ± 0.24
S2	1530.7	SVDI12-T14	15.19 ± 0.18